J. Mech. Phys. Solids 186 (2024) 105600

Contents lists available at ScienceDirect

Journal of the Mechanics and Physics of Solids

journal homepage: www.elsevier.com/locate/jmps

Thermal cracking: Clarifying the effects of phases, voids and grains through characterisation and crystal plasticity modelling

Wei Wang [a], Ruiqiang Zhang [a], Amir A Shirzadi [b], Daniel S Balint [a], Lee Aucott [c], Jun Jiang [a,*]

[a] Department of Mechanical Engineering, Imperial College London, London, SW7 2AZ, UK
[b] School of Engineering and Innovation, The Open University, Milton Keynes MK7 6AA, UK
[c] United Kingdom Atomic Energy Authority, Culham Centre for Fusion Energy, Culham Science Centre, Abingdon, Oxon OX14 3DB, UK

ARTICLE INFO

Keywords:
Thermal crack
Void
Grain boundary
Martensite
Crystal plasticity
Diffusion bonding

ABSTRACT

Thermally-induced cracking typically occurs during the cooling stage of various manufacturing processes, and is commonly seen in multiphase or the joints of dissimilar materials due to mismatch in their thermo-mechanical properties, such as thermal expansion, elastic-plastic deformation and, in some cases, phase transformation. However, the underlying cracking mechanism associated with local microstructure is still elusive. To improve the mechanistic understanding of thermal cracking, this work uses the diffusion-bonded 9Cr-1Mo steel as an example to study the key microstructural variables, such as interfacial phases, voids, grain boundary migration and crystallographic orientations. Meanwhile, a temperature-dependent crystal plasticity model coupled with a cohesive zone model is developed to provide more insights into the thermal-induced stress distribution at the grain scale. It is found that the stress at the void-free boundary of martensite and ferrite is dominated by shear, and its magnitude is insufficient to nucleate cracks. Whereas voids at phase boundaries can induce significant tensile stress, resulting in cracking at the phase boundaries as well as diffusion-bonded interfaces. Also, the occurrence of interfacial grain boundary migration plays an important role in local stress distribution. These microstructure features and their evolution are experimentally observed and used to verify the developed crystal plasticity models. These findings enhance the understanding of the influence of microstructure features on thermal cracking and provide a guide to designing and fabricating the microstructure with improved thermal crack resistance in various manufacturing processes.

1. Introduction

Welding (bonding) multi-phase or dissimilar materials could provide superior mechanical and/or multi-functional properties compared to metallic, single-phase materials (Lee et al., 2018; Ghoncheh et al., 2020). Manufactured multiphase or dissimilar metallic components have great potential in extremely demanding environments. For example, martensite and ferrite dual-phase steel exhibit high ultimate tensile strength and excellent formability, resulting in efficient sheet-forming processes for producing automotive components cost-effectively (Tasan et al., 2015). Also, in the nuclear fusion industry, multi-materials, such as CuCrZr alloy, W and SS316L are welded to withstand electromagnetic loads and neutron irradiation while providing strength and geometrical stability

* Corresponding author.
E-mail address: jun.jiang@imperial.ac.uk (J. Jiang).

https://doi.org/10.1016/j.jmps.2024.105600
Received 4 November 2023; Received in revised form 22 December 2023; Accepted 5 March 2024
Available online 11 March 2024

(Mazul et al., 2016). However, the two phases or metals often exhibit significantly different thermal and/or mechanical properties. As a result, the interfaces are often subjected to severe thermally-induced stresses (Fillafer et al., 2017), often leading to cracking and premature failure of components (Chu et al., 2010).

9Cr-1Mo steel is a commonly used martensite-ferrite dual-phase steel in the nuclear industry (Chatterjee et al., 2014). Some parts are joined by the diffusion welding method (Kazakov, 2013). During its cooling process, which is a complex thermal-metallurgical-mechanical process, thermal stress concentration at the joint boundary increases due to the mismatch in their coefficients of thermal expansion (CTE). In addition to thermal expansion, the cooling process of some multiphase steels, e.g., diffusion-bonded 9Cr-1Mo steel, is usually accompanied by martensite transformation (Chen et al., 2019). Phase transformation from austenite to martensite is driven by a diffusion-less process (Krauss, 1999). Due to martensite transformation during cooling, volume expansion occurs, resulting in an opposite volumetric change of another phase in the steel (Hwang et al., 2020), e.g., retained austenite or ferrite. Such anomalous plastic flow is so-called transformation plasticity, contributing to internal stresses at the grain level and local cracking (Erdogan and Priestner, 1999).

Although the mismatch in CTE, opposite volumetric change and transformation plasticity are the main reasons that induce local stresses, the existence of voids would further complicate the local stress state. Voids, as local defects acting as precursors of various failures, are commonly seen in advanced fabrications, including additive manufacturing (Marvi-Mashhadi et al., 2021; Vishnu et al., 2023; Pinz et al., 2022), diffusion bonding (Basuki et al., 2012; Zhang et al., 2015) and sintering (Zuo et al., 2022); however, the role that voids play under thermal loading is unclear, particularly when interacting with thermal cracks (e.g. in this work, thermal cracks were found crossing voids in a diffusion bonded 9Cr-1Mo steel sample). To distinguish the un-bonded interface and thermal cracks, the mechanism of diffusion bonding and the associated microstructure evolution described in (Hill and Wallach, 1989) are summarised in Fig. 1a. It is noted that the void tip is sharp in the initial stage (2) when the surface asperities come into contact. As atomic diffusion continues, the void closes. The void tips become more circular by continued diffusion, as shown in Fig. 1. The proposed cracking mechanism in Fig. 1a is consistent with the sharp crack seen in Fig. 1b which was generated by thermal cracking during the cooling process of the diffusion-bonded sample.

Prior modellings of the thermally-induced stresses in weldments were simplified by only considering the macroscopic level response without accounting for any microscopic crystallographic orientations, phases or voids due to the lack of appropriate mechanism models (Fillafer et al., 2017; Sugianto et al., 2009). For example, Yaghi et al. (Yaghi et al., 2008) simulated the stress evolution during the welding of P91 steel pipe, in which the phase transformation was considered by equivalent volumetric change and yield strength of phases. Finite element modelling did not take into account the responses from individual phases. More specifically, the localised deformation at grain/phase boundaries/voids and their interactions under thermal loading were ignored, which has been proved critical for microcrack initiation (Fillafer et al., 2017).

The crystal plasticity finite element (CPFE) method is widely used to capture grain-level mechanical responses (Wang et al., 2023). It can also depict the phase discrepancy by considering individual phase crystal structures (Xie et al., 2022) and their thermal-mechanical properties (Xu et al., 2022). The physics-based model is commonly used in CPFE to consider the temperature effects (Dunne et al., 2007). Based on this, temperature-dependent CPFE has been extensively used in crack initiation where stresses are generated all or in part by temperature change (Xu et al., 2022; Zhang et al., 2016; Ozturk et al., 2016). Moreover, the stress-strain response induced by thermal mismatch and grain-level elastic anisotropy was examined (Zheng et al., 2020). Nevertheless, CPFE modelling of thermal cracking and grain/phase boundary damage, like the example in Fig. 1b, is scarce, probably due to the requirement of a specific modelling method for phase boundary behaviours (Cai et al., 2022). The cohesive zone model (CZM) with traction-separation law is attractive (Tandogan and Yalcinkaya, 2022; Singh and Pal, 2020; Li and Chandra, 2003), because of its

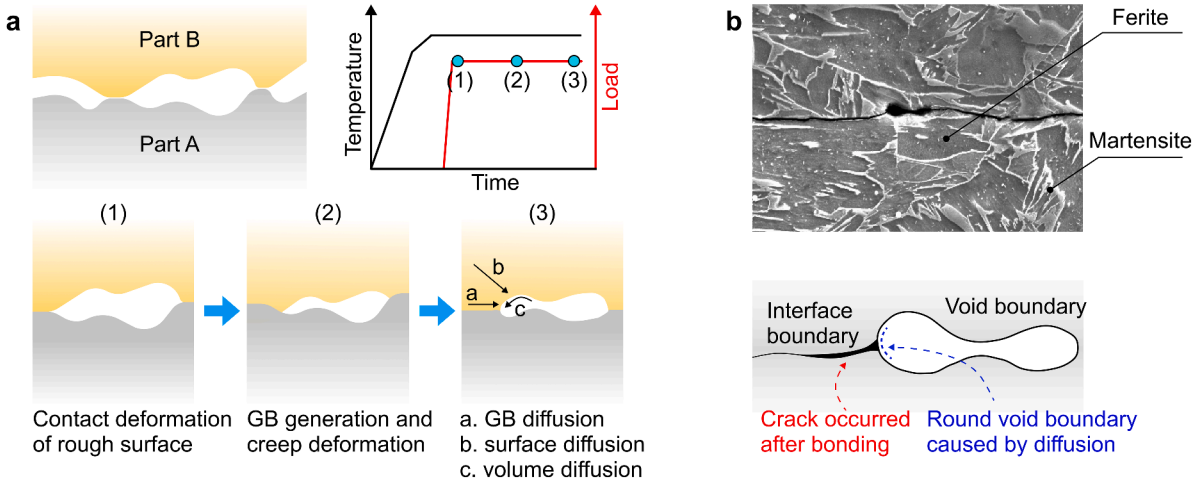

Fig. 1. Mechanism of voids closure and interfacial grain boundary cracking: (a) voids closure process and (b) evidence to show that the thermal cracking occurs after the diffusion bonding process.

capability to simulate microcrack initiation and failure of the phase/grain boundary, which has been combined with CPFE to examine the overall failure process from stress/stain concentration to fracture (Xu and Needleman, 1993; Alabort et al., 2018).

Thus, this study aims to establish a temperature-dependent CPFE coupled with CZM to provide insights into the thermal-stress-induced damage initiation, evolution and cracking in dual-phase steel, as well as investigate how underlying microstructure features, such as voids, phases and GBs, may affect the cracking behaviours. The proposed model and results are validated and supported by experimental characterisations of the samples fabricated by diffusion bonding. The effects of interfacial voids and their length, GB migration and grain orientation will be quantitively analysed and compared. The experimental and modelling results enhance the understanding of thermal crack formation and provide guidelines for improving thermal crack resistance in manufacturing.

2. Experimental method

2.1. Diffusion bonding process

The as-received material is commercial 9Cr-1Mo steel. The samples were first prepared by a diffusion bonding process. To obtain comparable results, the bonding surfaces of all samples were mechanically polished by SiC papers (up to P1200) and rinsed in propranolol before applying a load. The diffusion bonding was conducted in a vacuum with pressure just below 5×10^{-4} mbar. The heating rate and cooling rates were pre-set to be 1 °C/s. The bonding temperature was 900 °C with a compressive pressure of 15 MPa throughout the bonding cycle. The bonding temperature and pressure were maintained for 20 mins, 40 mins and 60 mins to reveal the effects of dwell time on the microstructure evolution.

The thermal cycle of diffusion bonding affects the microstructure evolution and phase transformation, since the phase transformation temperature (austenitisation process), A_1 (820 °C) 9Cr-1Mo steel (Yaghi et al., 2008) is lower than the bonding temperature (900 °C). When the temperature is held at 900 °C, a dual-phase microstructure comprising the ferrite and austenite phases is formed. The austenite phase was subsequently transformed into martensite during the cooling, according to Ref. (Yaghi et al., 2008), the martensite transformation starts at 375 °C and ends at 200 °C.

2.2. Microstructure characterization

The microstructure at the bonding interface was characterised by scanning electron microscopy (SEM) and electron backscatter diffraction (EBSD). SEM analyses were performed in a TESCAN CLARA scanning electron microscope. EBSD was performed using the

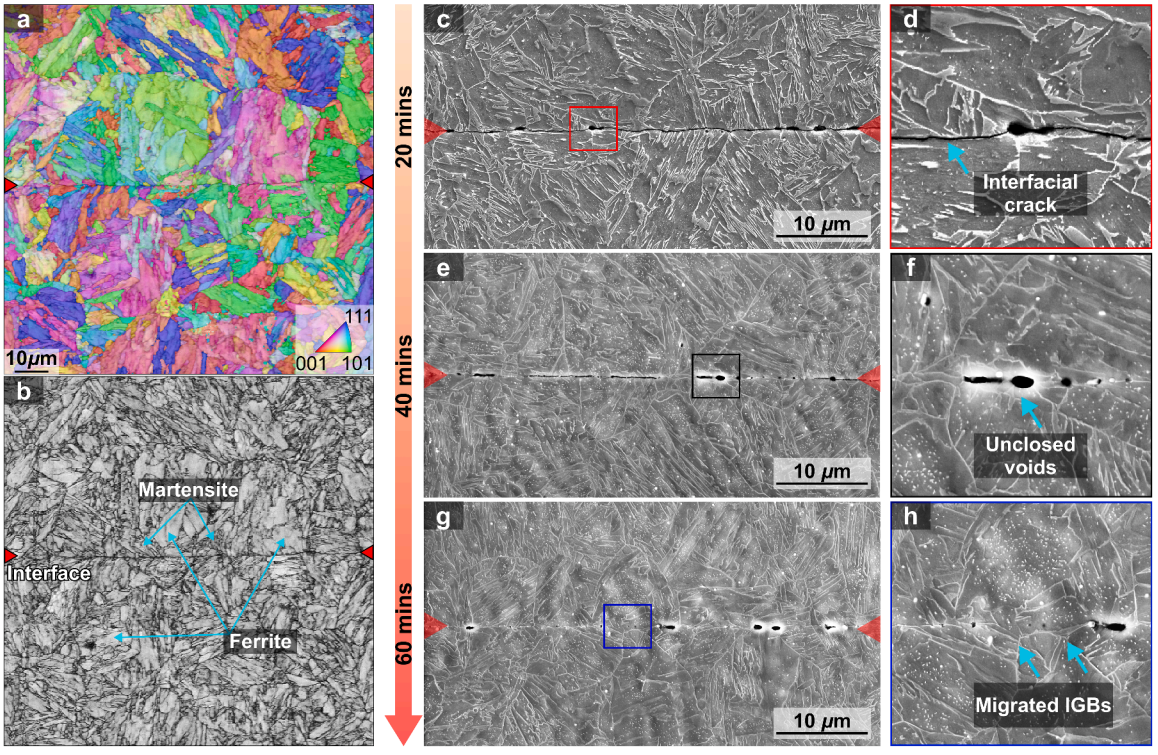

Fig. 2. Microstructure details of as-bonded 9Cr-1Mo steel after diffusion bonding at 900 °C: (a) EBSD-IPF map after 20 mins bonding, (b) EBSD-BC map after 20mins bonding, (c) and (d) SEM images after 20 mins bonding, (e) and (f) SEM images after 40 mins bonding, (g) and (h) SEM images after 60 mins bonding.

Oxford Instruments EBSD system. All samples were sectioned by electrical discharge machining (EDM) and metallographically ground by a series of SiC papers (up to P4000). To reveal the phase morphology, the samples were then electropolished for 30 s in a solution of 10 vol% perchloric acids in glacial acetic acid at room temperature at the voltage of 25 V. For EBSD analysis, the samples were electropolished for 60 s in the same solution at the voltage of 15 V. The SEM accelerating voltage for EBSD mapping was selected to be 30 kV, and the EBSD scanning step size was 0.15 μm.

Fig. 2 shows the interface microstructure of the as-bonded samples under three bonding conditions. The samples were characterized after diffusion bonding tests at room temperature. Fig. 2a and 2b are the EBSD-IPF (inverse pole figure) map and BC (band contrast) map acquired from the sample after 20 mins bonding. The fine martensite with dark colour in the BC map can be seen due to the high density of lattice defects within the martensite phase. The coarser ferrite grains were also identified with relatively bright colour. The microstructure evolution as a function of bonding time is shown in Fig. 2c-h. After 20 mins bonding, the bonding area shows a high fraction of connected interfacial grain boundary (IGB) cracks (see Fig. 2c and 2d), generating a long decohesion of the bonding interface. As the bonding time increases, the fraction of IGB cracks decreases. In addition to IGB cracks, voids closure and IGB migration are two main microstructural evolution processes. With bonding time increases, the voids fraction decreases and IGB migration fraction increases. This is attributed to the thermally activated mechanisms. The void closure is mainly achieved by atomic diffusion, which is promoted by the long bonding time with high bonding temperature. Considering the low bonding pressure was applied, the IGB migration is mainly achieved by the grain growth on the two sides of the bonding line. This long bonding time facilitates grain growth, resulting in a high fraction of IGB migration.

To compare the microstructures quantitatively, the fractions of IGB migration and voids are defined as shown in Fig. 3. As summarised in Fig. 3, the voids gradually close; meanwhile, IGBs migrate across the original bonding line. Whether the IGB migration and void closure are beneficial in resisting interfacial cracks during cooling is unknown. To clarify this question and reveal the associated underlying mechanism, the integrated CPFE-microstructure characterisation was systematically studied.

3. Modelling strategy

3.1. Crystal plasticity-based microstructural model

A temperature-dependent crystal plasticity model was used to capture the stress-strain response during cooling. This model has been developed to reveal the anisotropic elasticity and plasticity by considering an individual phase's elasticity modulus, crystal slip systems and thermal expansion coefficient. In the work, a dual-phase 9Cr-1Mo steel model comprising the martensite phase and ferrite phases was established.

The total deformation gradient $\mathbf{F}$ of both martensite and ferrite phases can be multiplicatively decomposed into the elastic $\mathbf{F}^{*}$, plastic $\mathbf{F}^{\mathrm{P}}$ and thermal deformation $\mathbf{F}^{\theta}$ gradients.

$$\mathbf{F} = \mathbf{F}^{*} \cdot \mathbf{F}^{\mathrm{P}} \cdot \mathbf{F}^{\theta} \tag{1}$$

The lattice deformation due to temperature change is described by

$$\dot{\mathbf{F}}^{\theta} = \dot{\mathrm{T}}\alpha_{th}\mathbf{F}^{\theta} \tag{2}$$

where T is the temperature and α_{th} is the isotropic coefficient of thermal expansion (CTE).

The plastic velocity gradient $\mathbf{L}^{\mathrm{P}}$ in the ferrite phase is determined by the shear slip rates $\dot{\gamma}^{\alpha}$ from all activated slip systems α.

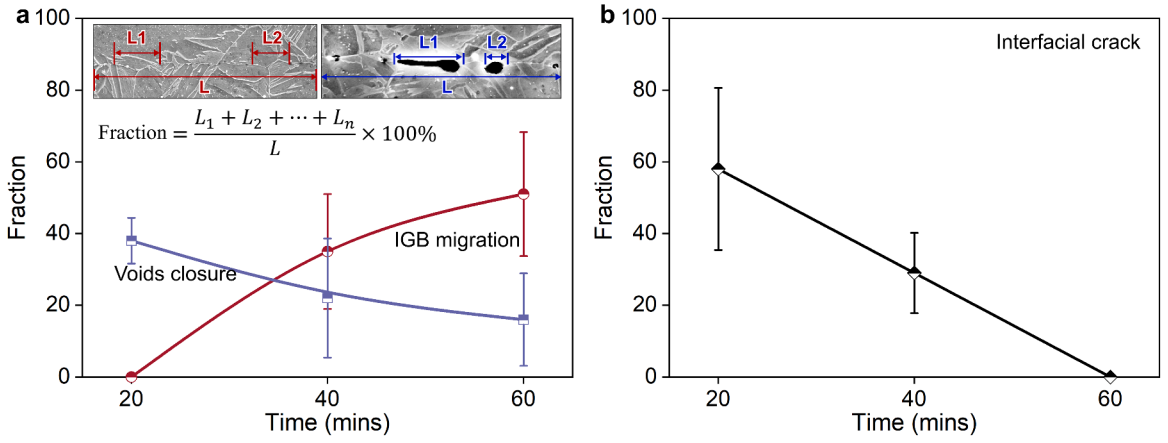

Fig. 3. Evolution of microstructure features with bonding time increase: (a) IGB migration and voids closure, and (b) interfacial crack.

$$\mathbf{L}^{\mathrm{P}} = \sum_{\alpha=1}^{\mathrm{N}} \dot{\gamma}^{\alpha} \mathbf{s}^{\alpha} \otimes \mathbf{m}^{\alpha} \tag{3}$$

where $\mathbf{s}^{\alpha}$ represents slip direction and $\mathbf{m}^{\alpha}$ is normal to the slip plane for the slip system α;N represents the total number of slip systems.

Following the approach of Voothaluru (Voothaluru et al., 2018), the contribution of martensite phase transformation is taken into account as an additional term in $\mathbf{L}^{\mathrm{P}}$:

$$\mathbf{L}^{\mathrm{P}} = \sum_{\alpha=1}^{\mathrm{N}} \dot{\gamma}^{\alpha} \mathbf{s}^{\alpha} \otimes \mathbf{m}^{\alpha} + \sum_{\chi=1}^{\mathrm{N}} \dot{\gamma}^{\chi} \mathbf{s}_{tr}^{x} \otimes \mathbf{m}_{tr}^{x} \tag{4}$$

where $\mathbf{s}_{tr}^{x}$ and $\mathbf{m}_{tr}^{x}$ are the transformation and habit vectors on the transformation system x. The shearing rate for each transformation system x is denoted by:

$$\dot{\gamma}^{\chi} = \gamma_{rt} \dot{f}^{x} \tag{5}$$

where γ_{rt} is a characteristic shear for transformation and $\dot{f}^{x}$ is the rate of volume fraction of martensite.

The relationship between the slip rate $\dot{\gamma}^{\alpha}$ and the movement of dislocations is described by a dislocation-based Orowan equation (Caillard and Martin, 2003), such that the slip rate on an individual slip system α is determined by

$$\dot{\gamma}^{\alpha} = \rho_{\mathrm{M}} \mathrm{b} \mathrm{v}^{\alpha} \tag{6}$$

where ρ_{M} is the mobile dislocation density, b is the magnitude of the Burgers vector, v^{α} is the velocity of dislocations, which is determined by thermally activated dislocation escape from obstacles such as lattice defects (Dunne et al., 2007). The slip rate $\dot{\gamma}^{\alpha}$ along the α slip system can be further expressed as

$$\dot{\gamma}^{\alpha} = \rho_{\mathrm{M}} \mathrm{b}^{2} \mathrm{v}_{0} \exp\left(-\frac{\Delta \mathrm{F}}{\mathrm{k_B T}}\right) \sinh\left(\frac{\Delta \mathrm{V}}{\mathrm{k_B T}} \left\langle |\tau^{\alpha}| - \tau_{\mathrm{c}}^{\alpha} \right\rangle\right) \tag{7}$$

where T is the loading temperature, $\mathrm{k_B}$ is the Boltzmann constant, v_0 is the jump frequency for dislocation escape, ΔF is the activation energy, ΔV is the activation volume, τ^{α} is the resolved shear stress and $\tau_{\mathrm{c}}^{\alpha}$ is the critical resolved shear stress. The shear strain rate $\dot{\gamma}^{\alpha}$ is only activated when resolved shear stress τ^{α} exceeds the critical resolved shear stress $\tau_{\mathrm{c}}^{\alpha}$, that is, $|\tau^{\alpha}| - \tau_{\mathrm{c}}^{\alpha}$. Otherwise, $\dot{\gamma}^{\alpha}$ remains inactivated.

A Taylor slip hardening rule is used for the evolution of critical resolved shear stress $\tau_{\mathrm{c}}^{\alpha}$ on the α slip system (Taylor, 1934)

$$\tau_{c}^{\alpha} = \tau_{\mathrm{c0}} + q_0 \mathrm{G} \mathrm{b} \sqrt{\rho_{\mathrm{SSD}} + \rho_{\mathrm{GND}}} \tag{8}$$

where G is the shear modulus of the material, τ_{c0} is the initial critical resolved shear stress without dislocation density hardening, q_0 is a dimensionless material-specific constant; ρ_{GND} is the density of geometrically necessary dislocations (GND); ρ_{SSD} is the density of statistically stored dislocations (SSD) determined by an equation using effective plastic strain as (Paramatmuni et al., 2021)

$$\dot{\rho}_{\mathrm{SSD}} = \lambda \cdot \dot{\mathrm{p}} \tag{9}$$

$$\dot{\mathrm{p}} = \left(\frac{2}{3} \mathbf{D}^{\mathrm{p}} : \mathbf{D}^{\mathrm{p}}\right)^{1/2} \tag{10}$$

where λ is the hardening coefficient and $\mathbf{D}^{\mathrm{p}}$ is calculated from $\mathbf{D}^{\mathrm{p}} = sym(\mathbf{L}^{\mathrm{p}})$.

The density of GND is calculated based on the Nye tensor, in which local plastic strain gradients supporting the lattice curvature are used

$$\boldsymbol{\Lambda} = \nabla \times \mathbf{F}^{\mathrm{p}} = \sum_{i=1}^{\mathrm{N}} \rho_{\mathrm{Gs}}^{\alpha} \mathrm{b}^{\alpha} \otimes \mathrm{s}^{\alpha} + \rho_{\mathrm{Get}}^{\alpha} \mathrm{b}^{\alpha} \otimes \mathrm{t}^{\alpha} + \rho_{\mathrm{Gen}}^{\alpha} \mathrm{b}^{\alpha} \otimes \mathrm{m}^{\alpha} \tag{11}$$

where $\rho_{\mathrm{Gen}}^{\mathrm{i}}$ is the normal component of the edge dislocation density, $\rho_{\mathrm{Get}}^{\mathrm{i}}$ denotes the tangential component of the edge dislocation density, and $\rho_{\mathrm{Gs}}^{\mathrm{i}}$ is screw dislocation component. Eq. (11) can be recast as

$$\mathrm{A} \rho_{\mathrm{G}} = \overline{\Lambda} \tag{12}$$

where $\overline{\Lambda}$ is the vectorized Nye's tensor and A is a linear tensor. The spatial gradient of plastic deformation was calculated on the Gauss points of each element with linear shape functions, as described in Ref. (Dunne et al., 2007). There are 72 independent dislocation components corresponding to the 24 slip systems in Eq. (11), which cannot be uniquely solved. A minimization problem is solved for the norm of the GND density subject to the constraints of Eq. (11). The norm is expressed as the sum of the squares of GND densities on each slip system according to Ref. (Cheng and Ghosh, 2015; Arsenlis and Parks, 1999; Xu et al., 2021).

$$\rho_{GND} = \sqrt{\sum_{i=1}^{N} (\rho_{Gs}^{\alpha})^2 + (\rho_{Get}^{\alpha})^2 + (\rho_{Gen}^{\alpha})^2} \tag{13}$$

The tetragonality of martensite depends on the carbon content. The body-centred cubic (BCC) crystal structure of martensite is validated when the carbon content is less than 0.6 wt% (Erdogan and Priestner, 1999). The carbon content of used 9Cr-1Mo steel is less than 0.1 wt%. Thus, the BCC crystal structure was used to describe the lattice structure of the martensite phase. <111>{110} and <111>{211} 24 slip systems in total are considered for both the martensite phase and ferrite phase. 24 transformation systems for martensite transformation are considered (Suiker and Turteltaub, 2005). The dislocation-based crystal plasticity constitutive law was implemented as a UMAT subroutine of a finite element code in ABAQUS (Dunne et al., 2007).

To calibrate the material properties of the two phases, the CPFE model was first used to simulate a simple uniaxial tensile condition. The virtual microstructures of the martensite and ferrite phases were defined by Neper (Quey et al., 2011). Based on the characterisation results shown in Fig. 2, the average grain size of ferrite is set to 30μm. The martensite phase exhibits a hierarchical microstructure in the EBSD map (Fig. 2a), in which three typical microstructure features corresponding to different length scales can be seen, namely the prior austenite grain boundary (PAGB), packets with polygonal shapes and strip-like blocks distributed in parallel. According to EBSD and SEM characterisation, the size of PAG was set to 30μm with three packets in each grain, and the block's width is 0.7 μm in each packet. The quasi-3D CPFE model subject to plane stress condition was used (Zhang et al., 2018) as shown in Fig. 4, in which the left, bottom and front surfaces are constrained by U_X=0, U_Y=0 and U_Z=0, respectively, while the front surface is free of any constraint. The material properties at room temperature are listed in Table 1. The tensile behaviour of the two phases is in good agreement with that in Ref. (Li et al., 2018) for 9Cr-1Mo steel.

The temperature dependant CPFE material properties for 9Cr-1Mo steel were then determined. The temperature dependant elastic properties of ferrite and martensite follow the linear equation according to Ref. (Fillafer et al., 2017)

$$E_F = \left(-\frac{8T}{95^{\circ}C} + \frac{3870}{19} \right) \text{GPa} \tag{14}$$

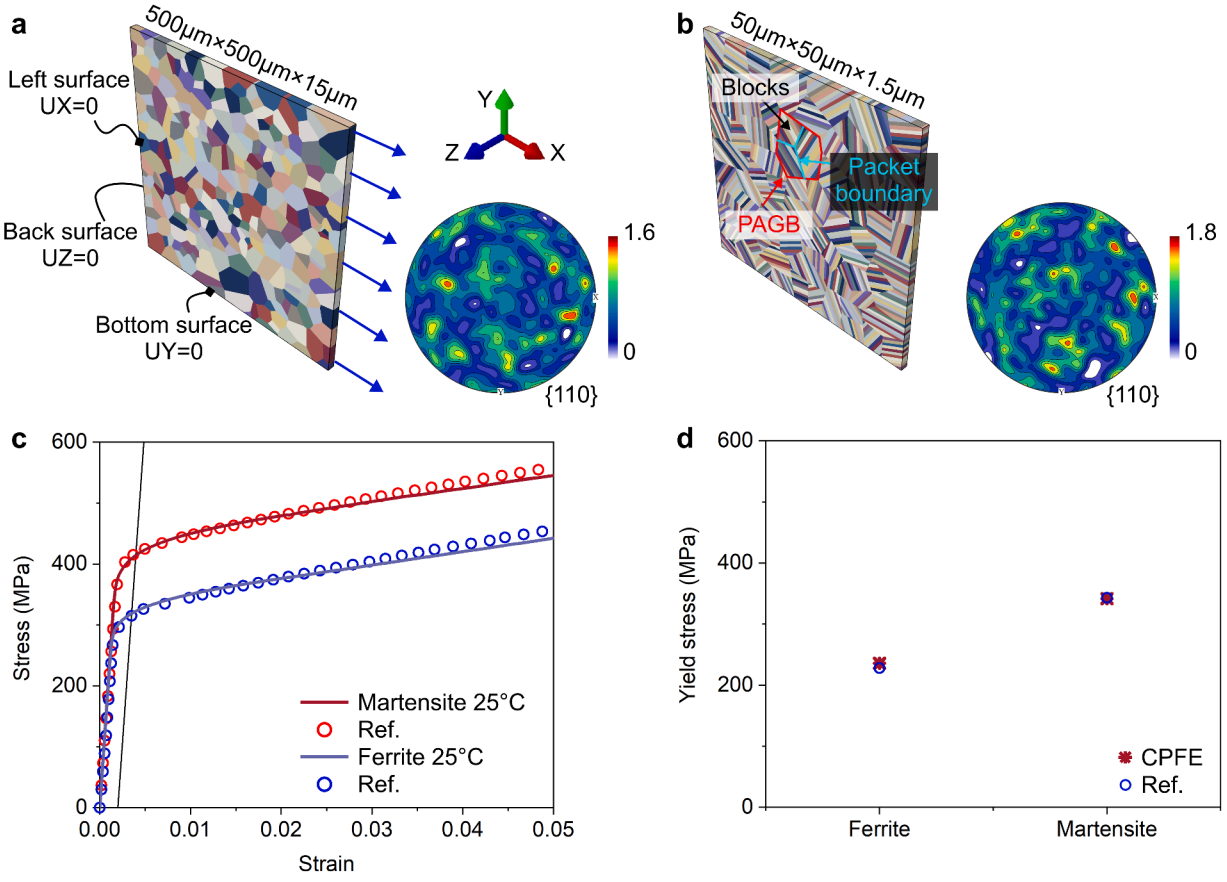

Fig. 4. CPFE model validation: (a) ferrite phase, (b) martensite phase and (c) comparison of tensile behaviours at room temperature, (d) comparison of yield strength at 375 °C.

Table 1
Material properties at room temperature used in CPFE.

Phase	C11 (GPa)	C12 (GPa)	C44 (GPa)	q_0	ΔV μm^3	ΔF (J)	k_B (JK^{-1})	λ (μm^{-2})	τ_c^α (MPa)	b (μm)	ρ_M (μm^{-2})
Martensite	276.6	118.6	79	0.1	40×b^3	2.60 × 10^{-20}	1.38 × 10^{-23}	60	168.1	2.5e-4	1 × 10^{-2}
Ferrite	271.4	116.3	77.5	0.37	40×b^3 (Wilson et al., 2019)	2.60×10^{-20} (Wilson et al., 2019)	1.38 × 10^{-23}	175	128.1	2.5e-4 (Wilson et al., 2019)	1 × 10^{-2} (Wilson et al., 2019)

$$E_M = \left(-\frac{9T}{95^\circ C} + \frac{3950}{19} \right) \text{GPa} \tag{15}$$

Shear modulus was obtained based on E from $G = E/(2(1+\upsilon))$, where υ=0.3 (Yaghi et al., 2008). Precisely obtaining critical shear strength at high temperature of single phase such as martensite and ferrite is challenging. This linear relationship of martensite and ferrite is commonly seen in the studies of martensite-ferrite steels (Li et al., 2018; Kang and Im, 2007). The critical shear strength in this study was first obtained according to the stress-strain curve in (Li et al., 2018), and then set to be linearly dependent on temperature according to Eqs. (16) and (17). The hardening parameters were kept constant with temperature, to reduce the complexity. The validation of yield strength at 375 °C is shown in Fig. 4d.

$$\tau_{c,M}^\alpha = (-0.1\text{T} + 170.6)\text{MPa} \tag{16}$$

$$\tau_{c,F}^\alpha = (-0.09\text{T} + 130.3)\text{MPa} \tag{17}$$

The martensite phase transformation and associated discrepancy in thermal expansion between martensite and ferrite are the main reasons for internal stress. Given the M_s and M_f temperatures of the selected steel are 375 °C and 200 °C, respectively, the calculation domain in this work focuses on the temperature range from 375 °C to room temperature (25 °C) (Fillafer et al., 2017). The representative finite element volume with martensite and ferrite phases is shown in Fig. 5. The volume consists of a hierarchical martensite matrix as described in Fig. 4b. The interfacial void with 3μm length and 1μm width was located at IGB in the region of interest (ROI). The differences in phase state (martensite or ferrite) would generate impact on the local deformation due to opposite volumetric change during cooling. For this reason, the grains with different phase states around void in Fig. 5 were modelled, and three cases (the case without a void, Type A where one side of the IGB is ferrite and Type B where both sides of IGB are ferrite) were considered to give a full understanding of the cracking mechanisms.

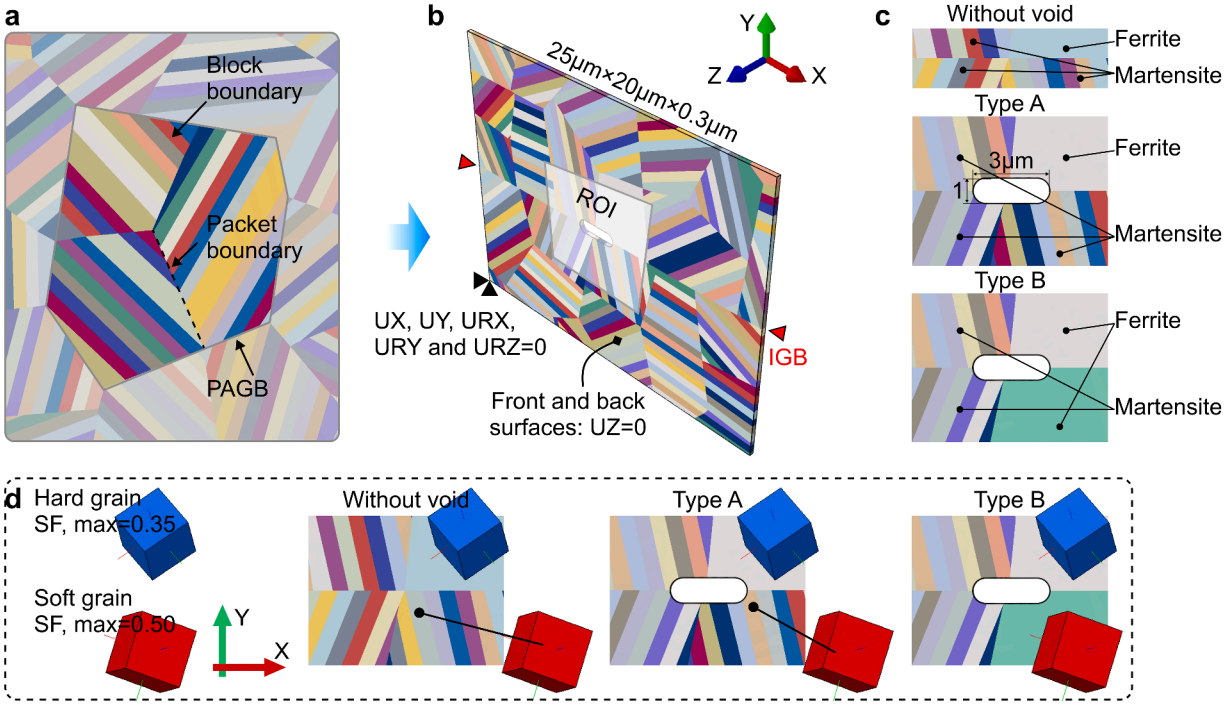

Fig. 5. Details of representative volume: (a) hierarchical structure of martensite, (b) boundary conditions and ROI, (c) three cases with different local microstructure in ROI, (d) orientation control in three cases.

The boundary conditions applied to the model are shown in Fig. 5b. The use of quasi-3D simulation is because of the target IGB morphology generated by diffusion bonding. It is noted that the IGB plane generated by diffusion bonding is parallel to the XZ plane. In such case, only three stress components σ_{yy}, σ_{xy} and σ_{yz} will contribute to the IGB cracking even in three-dimensional modelling. In addition, σ_{yy} and σ_{xy} are mainly discussed due to the negligibly small value of σ_{yz} (Fig. A1 in Appendix A). The rationale for this modelling strategy is discussed in Appendix A. The above assumptions are based on the unique IGB properties generated by diffusion bonding, the complex three-dimensional modelling should be considered where the grain boundary planes are randomly distributed.

The individual martensite blocks and ferrite grains orientations were assigned by three Euler angles. No global texture was considered in the model, as we focus on the local behaviour around the IGB. However, to obtain comparable results, the grains at the junction of martensite-ferrite-martensite or void boundary are controlled with the same orientations in all cases. The "soft-hard" grain pair was artificially induced, as depicted in Fig. 5d. The maximum Schmid factor (SF_{max}) of soft and hard grains was 0.5 and 0.35, respectively. The martensite phase transformation has been extensively investigated by finite element methods (Voothaluru et al., 2018; Manchiraju and Anderson, 2010; Moore et al., 2023). However, the finite element modelling was unable to illustrate the changes in grain morphology due to martensite phase transformation. It is noted that the grain morphology shows less impact on local mechanical responses than the orientation anisotropy (McCarthy et al., 2014). The phase transformation induced orientation anisotropy in an austenite grain can be modelled by the hierarchical microstructure approach. Therefore, this study adopted the hierarchical microstructure with BCC crystal structure from the beginning of the calculation (375 °C) of the martensite phase. This modelling method is capable of capturing the mechanical responses and thermal cracking behaviours induced by an individual martensite block.

During the temperature change in the calculation domain, the total strain is comprised of elastic deformation, plastic deformation, thermal expansion, volumetric change due to phase transformation and phase transformation plasticity (Yaghi et al., 2008). The thermal expansion can be described by α_{th} in Eq. (2). For the martensite phase, the thermal expansion and volumetric change due to phase transformation can be combined mathematically to obtain the overall effective thermal coefficient $\alpha_{th,M}$; this method has been successfully used in models of dual-phase steels (Yaghi et al., 2007; Suman and Biswas, 2020; Suman and Biswas, 2021; Yaghi et al., 2013). The volumetric change of 9Cr-1Mo steel has been reported as 3.75×10^{-3} (Yaghi et al., 2007). Thus, for the martensite phase, the strain rate induced by thermal expansion $\dot{\varepsilon}_T$ and volumetric change due to phase transformation $\dot{\varepsilon}_{VOL}$ can be expressed as

$$\dot{\varepsilon}_T + \dot{\varepsilon}_{VOL} = \alpha_{th}\dot{T} + 3.75\times10^{-3}\dot{f}^{x} \quad (M_f \le T \le M_s) \tag{18}$$

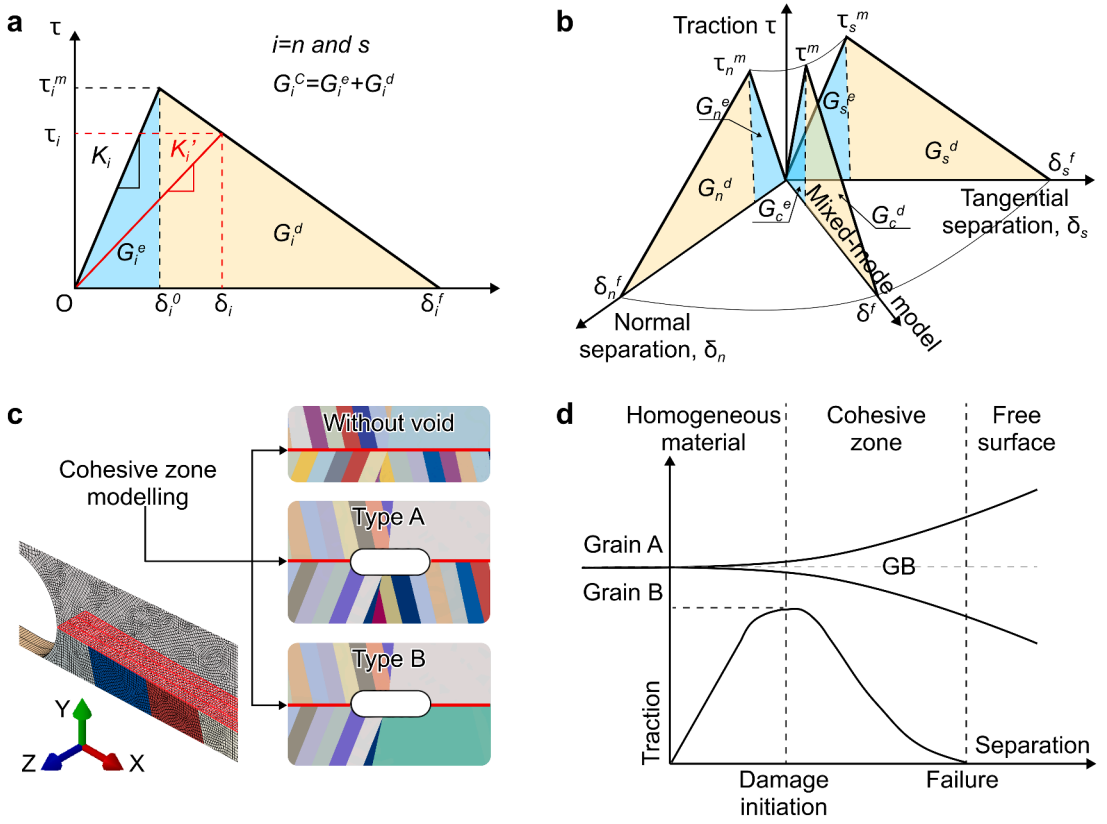

Fig. 6. Details of CZM: (a) bi-linear traction separation low and the nomenclature (Cai et al., 2022), (b) traction separation law for a normal load, shear load and mixed mode load (Cai et al., 2022), (c) setting of the integrated CPFE-CZM model and (d) IGB damage principle (Alabort et al., 2018).

where f^x ranges from 0 to 1, linearly with temperature. Thus, the overall CTE of martensite $\alpha_{th,M}$ is -0.84×10^{-5} ($M_f \le T \le M_s$) and 1.3×10^{-5} ($T \le M_f$) (Schröder, 1985). CTE of the ferrite phase $\alpha_{th,F}$ is set to be $1.4 \times 10^{-5}\ K^{-1}$ throughout the calculated domain (Schröder, 1985). The phase transformation induced plasticity of the martensite phase is captured by Eqn. (4). The changes of CTE with temperature are not considered in this study, due to the practical challenge of precisely obtaining the changes of CTE of individual phases. The necessary simplifications enabled us to conduct simulations and focus more on the effects of microstructure features rather than the materials constant itself.

4. Interfacial grain boundary damage model

Thermal cracking behaviour at the diffusion bonding interface was modelled by a cohesive zone model (CZM). The method is often used to model boundary cracks in metallic materials, such as nickel-based superalloy (Alabort et al., 2018), twinning–induced plasticity steel (Cai et al., 2022) as well as 9Cr-1Mo steel (Mahler and Aktaa, 2015; Mahler and Aktaa, 2016). CZM can describe normal and shear stress localisation around the interface. The material interface will enter the damage stage when the local stress reaches the threshold, eventually initiating a crack. In this work, interfacial grain boundaries were assumed to follow a bi-linear traction-separation law (TSL), as shown in Fig. 6a (Cai et al., 2022). The GB was defined to be purely elastic with stiffness K_i until damage begins. When the traction force reaches the predefined threshold τ_i^m, based on a damage initiation criterion, the GB will enter the damage stage during which the stiffness of the grain boundary reduces with increasing separation δ_i. The IGB cracks will eventually initiate when the separation δ_i reaches the threshold value δ_i^f.

According to the TSL, the evolution of stress due to damage can be written as:

$$\tau_i = (1-d_i)K_i\delta_i \tag{19}$$

where $i = n\ and\ s$ represents the normal and shear direction; d_i is the stiffness damage factor, which is defined based on the energy criterion in the damage stage

$$d_i = \frac{\delta_i^f\left(\delta_i^{max}-\delta_i^0\right)}{\delta_i^{max}\left(\delta_i^f-\delta_i^0\right)} \tag{20}$$

where the δ_i^f is a critical separation when cracking occurs, δ_i^{max} refers to the maximum value of the effective separation achieved during the loading history, and δ_i^0 is the separation when the damage initiates. The relationship between δ_i^f and cohesive energy G_i^C can be described as

$$\delta_i^f = 2G_i^C/\tau_i^m \tag{21}$$

Considering the complex stress state near the interface especially when microvoids exist, the TSL for the mixed-mode loading is illustrated in Fig. 6b (Cai et al., 2022). The maximum stress values τ_n^m and τ_s^m are the threshold stress for damage initiation, and the critical cohesive energy G_n^C and G_s^C are the threshold for cracks in the normal and shear directions, respectively. The quadratic nominal stress criterion (QUADS) considering the contribution from both normal and shear is

$$\left\{\frac{\langle\tau_n\rangle}{\tau_n^0}\right\}^2 + \left\{\frac{\tau_s}{\tau_s^0}\right\}^2 = 1 \tag{22}$$

where the Macaulay bracket guarantees that the normal stress τ_n is positive, while compression does not initiate damage. QUADS=1 represents damage initiation and GB softening. The damage variable (SDAG) evolution during softening is described by a power low as

$$\left\{\frac{G_n}{G_n^C}\right\}^\lambda + \left\{\frac{G_s}{G_s^C}\right\}^\lambda = 1 \tag{23}$$

where λ is an exponent that is set to unity according to Ref. (Cai et al., 2022). G_n^C and G_s^C are the cohesive energy under normal and shear loading modes.

Damage initiation is defined by QUADS, following Eq. (22). Considering that the elastic stiffness of the IGB should be higher than that of the grain interior, the elastic stiffness of IGB at room temperature is thus defined by $K_n = 210\text{GPa},\ K_s = K_n/(2(1+v))$ (Simonovski and Cizelj, 2013). The temperature-dependent K_i follow the same trend of martensite phase shown in Eq. (15), $K_n = \left(-\frac{9T}{95^\circ C} + \frac{4035}{19}\right)\text{GPa}$. The threshold of stress for damage initiation is normally defined as 1 to 4 times of yield strength (Chen et al., 2013). Therefore, in the current work $\tau_n = 546\text{MPa} \approx 1.3\sigma_{0.2,M}$ (Recall Fig. 4c), and $\tau_s = 0.33\tau_n$. The cohesive energy G_i is estimated by (Alabort et al., 2018)

$$G_i = \frac{K_c^2(1-v^2)}{E} \tag{24}$$

Where K_c is the stress intensity factor, which is set to be $24\text{MPa}\cdot\sqrt{\text{m}}$. The cohesive energy G_i and stress threshold τ_i were kept as constants throughout the calculation domain to reduce the input parameters.

The integrated CPFE-CZM model can describe the deformation behaviours of both grain interior and GB. Specifically, the

temperature-dependent CPFE can capture stress and strain localisation and slip activation under thermal loading. At the same time, CZM determines the damage of GB and updates the stress state with CPFE. It is noted that the IGB generated by diffusion bonding is always considered a weak point due to local defects such as microvoids and element depletion, which provide the potential cracking path. For this reason, the present study mainly focuses on the cracking of IGB. By adopting this computational framework, the CPFE-CZM model for three defined cases is shown in Fig. 6c. Fig. 6d illustrates the damage principle from initiation to propagation to final cracking in a specific IGB.

5. Results and discussion

5.1. Interfacial grain boundary behaviours

Fig. 7 shows the interfacial behaviour in the absence of any interfacial voids. The distributions of normal σ_{yy} and shear stress σ_{xy} in Fig. 7a are obtained at the temperature where damage initiates, as indicated in Fig. 7c. Both normal σ_{yy} and shear stress σ_{xy} concentrate at the triple junction of the IGB. This site involves different phases adjacent to each other (phase boundary), where the mismatch of thermal expansion and the crystallographic misorientation are the main causes of the elevated stresses. Fig. 7b gives the stress profiles on path A-A', which clearly shows that the shear stress component σ_{xy} reaches its maximum of 150 MPa at the triple junction and reduces as the distance from the triple junction increases. In comparison, the normal stress σ_{yy} at the triple junction is 50 MPa, far less than the shear stress. Its magnitude gradually increases with distance, eventually reaching a plateau of about 100 MPa. Considering the stress field along the A-A' path shown in Fig. 7a and b, Fig. 7c show the damage value (QUADS) along the A-A' path as a function of temperature. The damage initiates at the triple junction when the temperature is reduced to about 280 °C. The length of damaged IGB gradually increases as the cooling continues and stops at 1.32μm at room temperature (25 °C).

The damage processes and the cracking behaviours of all three cases (without void, Type A and Type B with voids) are presented in Fig. 8. First, the crack doesn't initiate in the case without the void, and the maximum SDAG is only about 0.8 at the triple junction (Fig. 8a), implying that the IGB would be safe if no voids or other defects exist. In contrast, thermal cracking occurs in both Type A and B (Fig. 8b and c) containing a micro-void, implying the adverse effects of interfacial voids on IGB damage. Recall that the grain on one side of IGB is martensite and another side is ferrite in Type A, unlike Type B where grains on both sides are ferrite. Even though the results shown in Fig. 8b and c indicate thermal cracks in both Type A and B regardless of the phase state around the void, the cracking behaviours of these two types are different, which is discussed in the following sections.

The stress localisations in Type A and B interfaces were further analysed to reveal the underlying cracking mechanism induced by the void. Fig. 9a illustrates the stress distributions of Type A and Type B interfaces. Both σ_{yy} and σ_{xy} are concentrated at the void boundary in Type A. Different from the case without the void, the concentration of σ_{yy} in Type A is more pronounced than that of the σ_{xy}, as illustrated in Fig. 9b. The maximum σ_{yy} is about 280 MPa at the void boundary. In contrast, the maximum σ_{xy} is about 100 MPa and both reduce with distance away from the void boundary. Compared with the case without void, the shear stress σ_{xy} induced by the phase boundary still exists in Type A. In addition, the void introduces a high magnitude of σ_{yy} at IGB. In Type B, the grain on the two sides of IGB is set to be ferrite. Without the phase boundary at the IGB, the shear stress σ_{xy} is rather negligible. However, the normal stress σ_{yy} is found to be more severe, reaching about twice that in Type A interface (Fig. 9b). It is known that the martensite phase transformation during cooling induced expansion, which is an opposite volumetric change of the ferrite phase. In the case with martensite and ferrite (Type A), the opposite volumetric change between two phases generates shear near the void edge. In the case with ferrite only, the expansion of the surrounding martensite phase induces the tension on the ferrite phase, resulting in the high level of tensile stress.

From the results shown in Figs. 7–9, the stress state at the IGB during cooling with and without considering the interfacial voids is

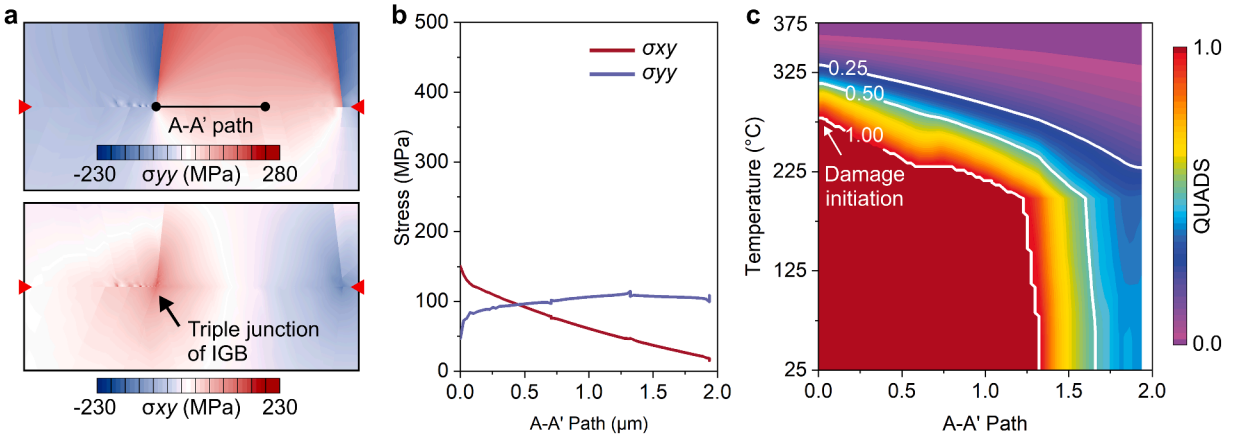

Fig. 7. IGB behaviours in the case without void: (a) normal σ_{yy} and shear stress σ_{xy} at the temperature where damage initiates, (b) line results of normal σ_{yy} and shear stress σ_{xy} at the same temperature of (a), (c) QUADS distribution along with IGB with the change of temperature.

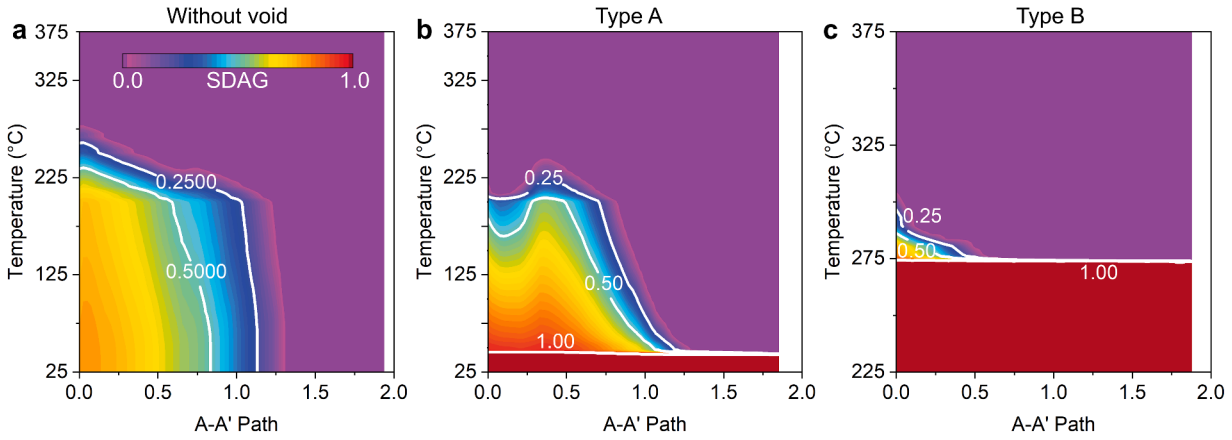

Fig. 8. damage processes and the cracking behaviours of three cases corresponding to Fig. 6c: (a) without void, (b) Type A and (c) Type B.

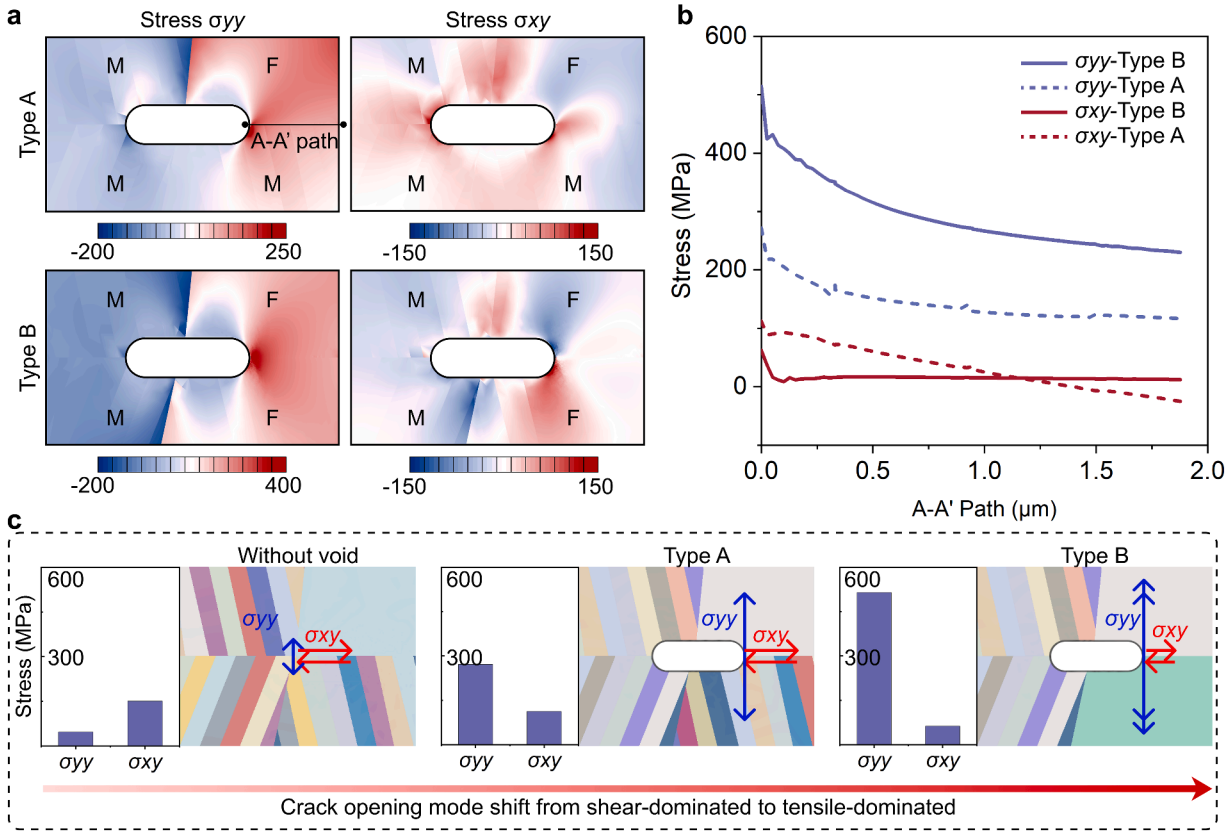

Fig. 9. Stress state at IGB during cooling: (a) distributions of σ_{yy} and σ_{xy} in Type A and B at 280 °C, (b) line results in path A-A' according to Fig. 9a, (c) summary of stress opening mode for the cases without void and Types A and B with voids.

revealed: First, the existence of the phase boundary induces a shear stress concentration, but the magnitude is not enough to open a crack under the calculated condition. Second, the interfacial voids trigger severe normal stress σ_{yy} at the void boundary in both Type A and Type B interfaces, which is the main cause of IGB thermal cracking. The stress state for IGB thermal crack opening is summarised and presented in Fig. 9c.

The stress evolution in Type A and B reveals the relationship between the stress components and IGB thermal cracking behaviours. Fig. 10a and d show the QUADS in Types A and B. Considering that the crystallographic orientations of grains in the two types are the same, the thermal-induced IGB damage is due to the different stress states in the two types. The evolutions of normal stress σ_{yy}, overlaid with the contour lines of QUADS=1, are shown in Fig. 10b and e. The damage initiation along with the IGB (refer to the contour lines of

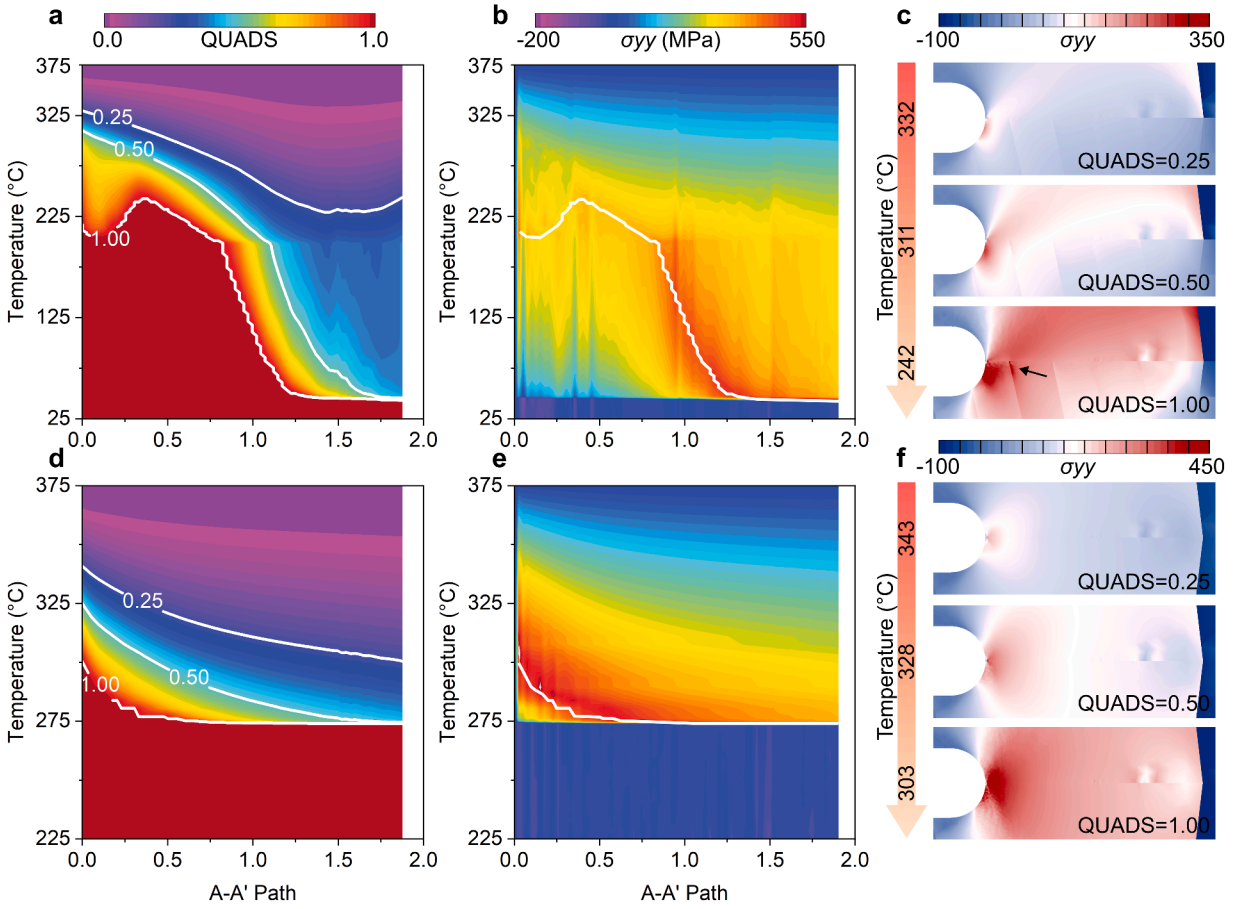

Fig. 10. Relationship between IGB damage behaviours and stress: (a) and (d) show evolutions of QUADS; (b) and (e) are evolutions of σ_{yy}, (c) and (f) are distributions of σ_{yy} at three typical moments. (a), (b) and (c) are results of Type A; (d), (e) and (f) are results of Type B.

QUADS=1) shows good agreements with the maximum value of σ_{yy}, which provides compelling evidence of the dominant role played by σ_{yy} in thermal-induced IGB crack initiation and evolution in both Type A and B.

From the results in Fig. 8, the IGBs of both types are expected to be damaged and eventually cracked before cooling to room temperature. However, the damage or crack initiation and propagation in the two types are very different. The damage initiates at 242 °C in Type A (Fig. 10a), introducing IGB thermal cracking at 45 °C (Fig. 8b). In contrast, for Type B, the temperatures for damage initiation and cracking are 303 °C (Fig. 10d) and 275 °C (Fig. 8c), suggesting that in Type B, IGB has less damage resistance than Type A. The different cracking behaviours caused by the phase state between Type A and B are explained below. First, the magnitude of σ_{yy} in Type B is much higher than that in Type A, especially near the void boundary (also see Fig. 9b). Second, the morphology of martensite and ferrite is different. As shown in Fig. 10c and F, the σ_{yy} concentrates more in a local area near the void boundary in the single ferrite grain in Type B at three typical moments (QUADS=0.25, 0.5 and 1), while σ_{yy} in Type A shows a less concentrated distribution with continued cooling because of the interactions between martensite blocks (black arrow in Fig. 10c). The maximum value of σ_{yy} has moved to the position 0.45 μm away from the void boundary at 251 °C (Fig. 10b).

5.2. *Effects of interfacial grain boundary migration*

The effects of IGB migration on interfacial thermal cracks are studied in this section. The statistical results in Fig. 3a show that as the dwell time increases, the fraction of IGB migration increases while the fraction of interfacial cracks decreases. This implies the potential correlation between IGB migration and the reduction in thermal cracking. Fig. 11 provides more intuitive and evident traits which support the above-mentioned correlation. In Fig. 11a, the IGB migration occurs with the martensite phase within the grain. The martensite blocks are parallel but tilt toward the IGB plane. It is readily seen that the IGB thermal cracks stopped when it encountered migrated IGB (martensite phase). However, Fig. 11c shows that the crack first encountered the ferrite phase in the grain with migrated IGB. The crack passes through the ferrite phase but stops in front of the martensite phase, as shown in the enlarged figure in Fig. 11c. Another feature induced by IGB migration is that the crack path changes and follows the substructure boundary of the grain, as shown in Fig. 11e. The schematic diagrams in Fig. 11 illustrate proposed crack propagation mechanism.

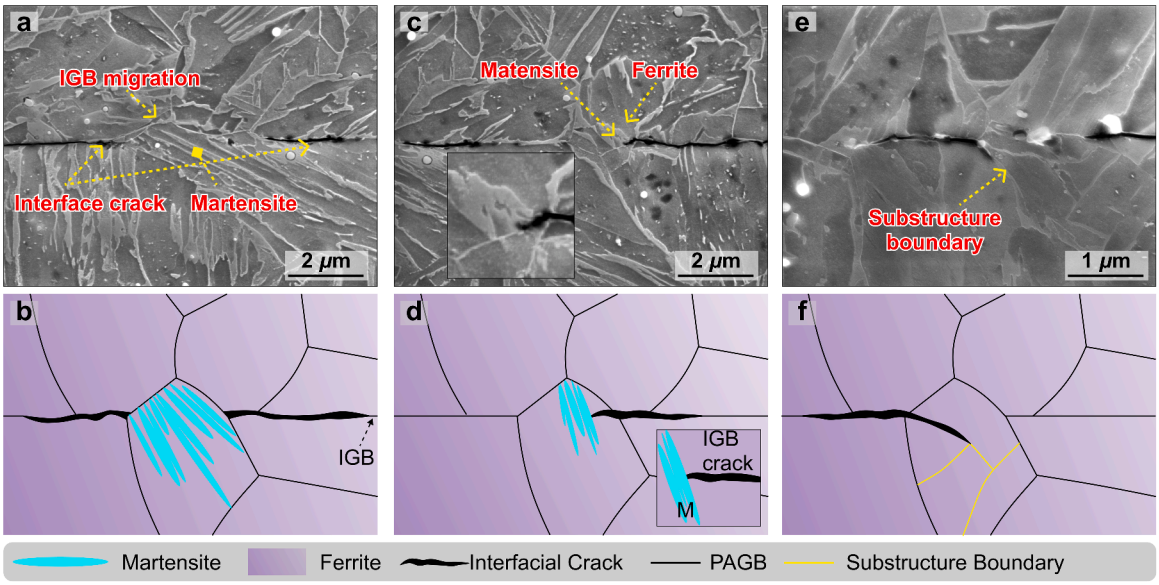

Fig. 11. Three microstructure features with respect to the effects of IGB migration on interfacial cracking: (a) and (b) show crack propagation stopping when it encountered a migrated IGB with martensite, (c) and (d) show the crack path through the ferrite but stopping in front of the martensite, (e) and (f) shows the crack following the substructure boundary of grain.

To further understand the IGB migration and thermal cracking correlations shown in Fig. 11, the CPFE-CZM model was used accordingly. As shown in Fig. 12a, based on the grain morphology in Fig. 5b, the migrated IGB is initiated on the right side of the void. The grain orientations of ferrite and martensite blocks at the void boundary were controlled to be a "hard-soft" grain pair, the same as with Type A in Fig. 5. The grain with migrated GB was subdivided into martensite blocks, which are perpendicular to the IGB plane. Two types were considered according to the experimental observation shown in Fig. 11a and c, named Type C and Type D. In Type C, the phase of the grain with migrated GB is full martensite blocks corresponding to the phase distribution in Fig. 11a. In Type D, the first block on the left side of grain with migrated GB is set to be the ferrite phase, which the IGB crack will first encounter during cooling according to the phase distribution in Fig. 11c. It is noted that the different cracking resistance shown in Fig. 11(a) and (b) is no doubt owing to the different inner strengths of the two phases. Nevertheless, more insights are provided on external thermal mechanical responses and associated stress state-cracking due to IGB migration and phase state. To obtain comparable results between Type C and Type D, the damage and crack criteria are the same for both IGB and grain interior, as shown in Fig. 12b. The differences in crack resistance of GB and grain interior are not considered in Type C and Type D, but different stress states (Fig. 13) and cracking behaviours (Fig. 12(e) and (F)) can be obtained based on the model, which allows us to correlate the IGB migration-phase state to stress state-cracking behaviours.

Fig. 12c shows the damage variation along the B-B' path of Type C after cooling to room temperature. The phase map is overlayed to show crack behaviours with different phases. Results indicate that the crack (where SDAG=1) stops when it encounters the migrated IGB with the martensite phase. The SDAG gradually decreases through the martensite interior and eventually drops to zero. On the contrary, the crack propagates through the ferrite phase (SDAG=1) in the grain with migrated GB in Type D (Fig. 12d), but it is hindered by the martensite phase with the decreases in SDAG. Results in Fig. 12c and d show good agreements for each selected phase distribution to the experimental observations obtained in Fig. 11. Moreover, the IGB damage evolutions in Type C and D captured by the model are shown in Fig. 12e and F. The damage initiates at about 225 °C in both types, which is not influenced by the phase distribution.

The IGB cracking behaviours shown above are strongly influenced by the IGB migration and predominantly because of their phase distribution in the grain with migrated GB. The intrinsic effects of IGB migration and associated phase distribution on the stress state are further discussed in Fig. 13. The evolution of normal σ_{yy} and shear stress σ_{xy} in Type C at IGB (refer to F/M interface in Fig. 13) follow the same rule as described in Section 4.1 and the damage initiation is dominated by the normal component σ_{yy}. However, the normal stress diminishes sharply at the triple junction of migrated GB, and then explicitly exhibits lower or negative σ_{yy} in the martensite blocks, which would contribute less to crack opening. The shear component σ_{xy} at the martensite phase is relatively higher due to the thermal expansion mismatch induced by the phase boundary, but the σ_{xy} alone at the interface is insufficient to open a crack, as discussed in Section 4.1. Fig. 13c explicitly shows stress components and QUADS variation along the B-B' path at 325 °C. The predicted stress histories in Type D are shown in Fig. 13d, e and F. The ferrite interior exhibits considerable σ_{yy} at the beginning of the damage initiation (Fig. 13d). This is because thermal expansion and phase transformation of the martensite phase would induce the internal loading expected to be accommodated by the relatively soft ferrite phase. Consequently, the internal stress for both normal σ_{yy} and shear σ_{xy} components are high in the ferrite grain, as depicted in Fig. 13d and e, which further generates grain damage (Fig. 13f) and a crack path for IGB cracking.

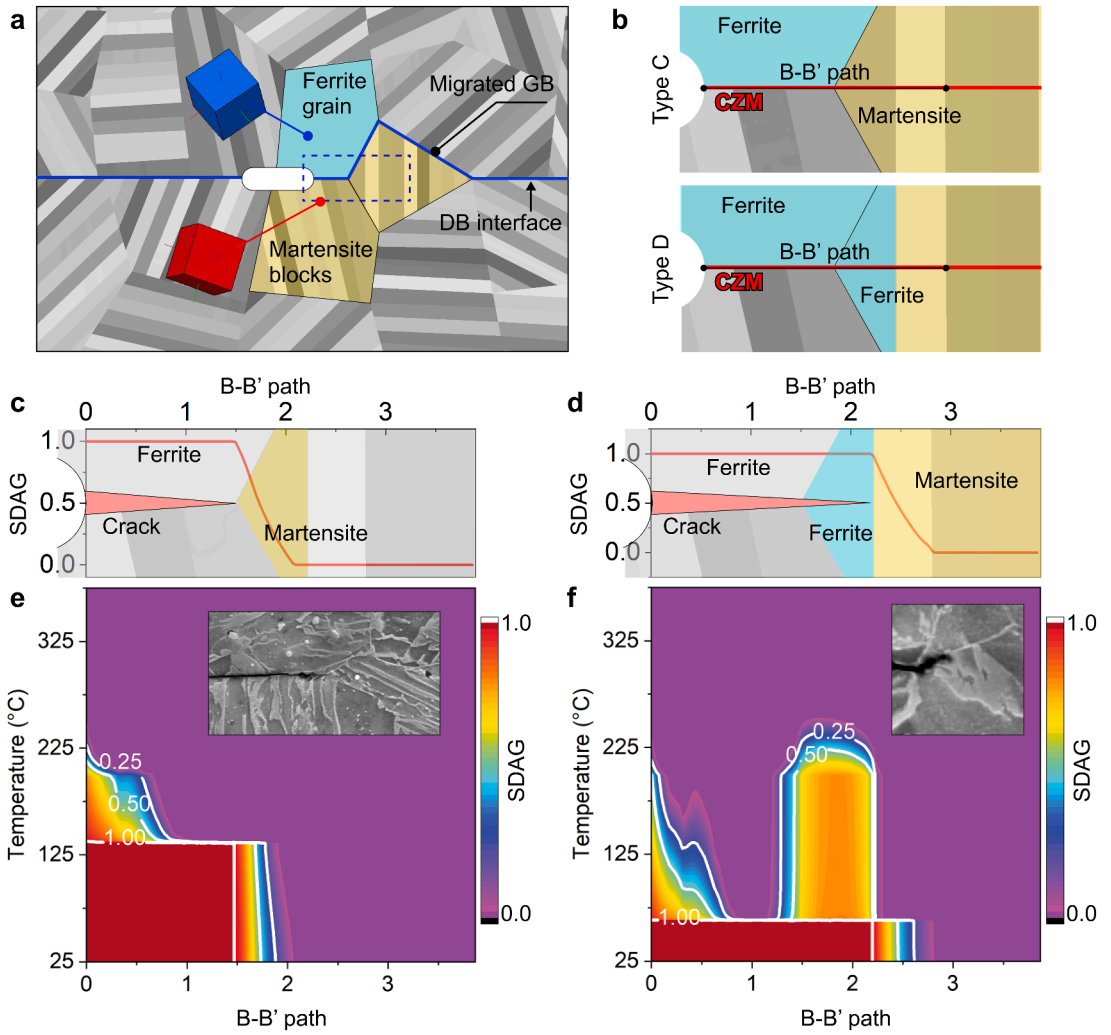

Fig. 12. Model details and cracking behaviours considering the IGB migration: (a) grain morphology, (b) two types with different phase distribution, (c) SDAG of Type C after cooling with phase distribution overlayed, (d) SDAG of Type D after cooling, (e) SDAG evolution of Type C, (f) SDAG evolution of Type D.

5.3. *Effects of void closure*

The effects of void closure on thermal cracking are presented in Fig. 14. It is known that void closure during diffusion bonding mainly refers to the reduction of length driven by atom flux due to the gradient of chemical potential. The models with three lengths of void (3μm, 2μm and 1μm) were thus established based on the grain morphology of Type A shown in Fig. 5b. To obtain comparable results, the orientations of the ferrite grains and martensite blocks on the right side of the void are kept the same as shown in Fig. 14a. The thermal cracking behaviour seems to correlate with the existence of voids, due to the highly concentrated normal stress σ_{yy} on the void boundary. The evolution of σ_{yy} in the cases with 1μm and 2μm void is thus shown in Fig. 14b and c. Compared with the 2μm void, the 1μm void introduces a moderate σ_{yy} at the void boundary from the beginning of the damage initiation (about 275 °C in Fig. 14b). Consequently, the case with 1μm void shows a short length of IGB that suffers damage (1.6μm) compared to the 4.1μm (which passed through the whole ferrite/martensite interface) in 3μm void case. More importantly, as summarised in Fig. 14f, the length of the crack reduces with voids closure. The length of the crack is 0.9μm in the 2μm void case, which is three times shorter than that of the 3μm void case. No crack occurs in the case with a void that shrinks to 1μm, which gives qualitative results and theoretical guidance to improve the joint mechanical properties. The correlation between voids closure and IGB cracking implied by characterisation in Fig. 3 is thus confirmed by the simulation results in Fig. 14.

5.4. *Effects of crystallographic orientation*

The results in Section 4.1 suggest a strong correlation between the phase distribution and thermal crack initiation, which could

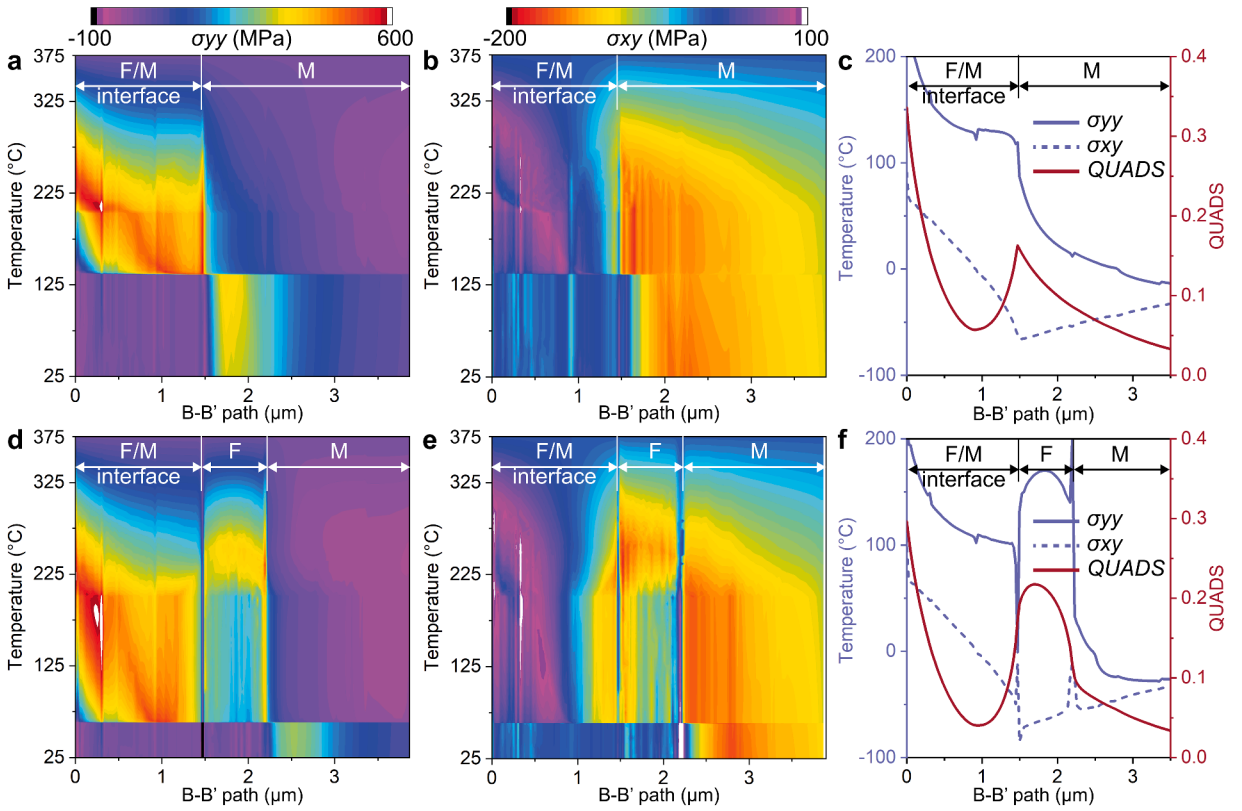

Fig. 13. Evolution of stress components and IGB damage with respect to the effects of IGB migration: (a) and (b) σ_{yy} and σ_{xy} in Type C, (c) line results of σ_{yy}, σ_{xy} and QUADS in Type C, (d) and (e) σ_{yy} and σ_{xy} in Type D, (f) line results of σ_{yy}, σ_{xy} and QUADS in Type D.

eventually lead to IGB thermal cracks. The intrinsic reason behind this is the change in the stress field, which stems from the combination of different phases on the two sides of the IGB so as to affect IGB damage. The stress field in the local area around voids is in the length scale of the grain size; the micromechanical response from that scale is sensitive to the crystallographic orientation. This section thus further examines the crystallographic sensitivity of IGB damage. Fig. 15a indicates the grain orientations in Type A and Type E. Based on the orientations in Type A, the ferrite grain in Type E is set to be the same as the martensite block, with the 'soft' orientation along the *y* direction. It was found that the change in orientation of ferrite grain activates different slip systems in the adjacent martensite blocks. In the current work, the slip system with the largest and the second largest strain value was determined as the primary and the secondary slip. Considering the complex stress state induced by thermal-mechanical history, Fig. 15b separately illustrates the primary and secondary slip field of the martensite block at about 280 °C in both types, results from which show that the primary and secondary activated slip systems in Type A are different from those in Type E. It is notable that the slip fields in Type A generate a large plastic zone where the activated slip systems promote long-range dislocation slip, from the void boundary to the boundary between Block A and Block B (white arrow in Fig. 15b). Hence, the IGB damage in Type E is obviously different from Type A (Fig. 10a), as shown in Fig. 16a. The evolutions of σ_{yy} are shown in Fig. 16b. In Type A, the maximum value of σ_{yy} along the IGB gradually moves to the boundary of Block A/B due to the pile-up of long slide dislocations. However, the activated slip systems in Type E generate a highly concentrated σ_{yy} at the void boundary, adversely damaging the IGB so as to generate the crack in the early stage of cooling (Fig. 16a). The damage initiation behaviours at the void boundary and boundary of Block A/B are shown in Fig. 16c. The damage induced by thermal loading is sustained by a long IGB in Type A, which thus show a better crack resistance.

In addition to Type A and Type E, the grain pairs with different misorientations of IGB have been examined. The misorientation of the tested IGBs covers the full range of misorientation in BCC crystal structure, ranging from 10° to 60° To reduce the indeterminacy, the orientation of Grain C is fixed. The Euler angles and misorientation used are summarized in Table 2. As shown in Fig. 17, no direct relationship was found between the observed IGB damage process/cracking behaviours and grain boundary angle. Nonetheless, the IGB in all 8 cases suffers cracking, and the average cracking moment is when the temperature drops to about 143 °C, with a standard deviation of 59 °C.

The quantitative results of microstructure effects on IGB cracking are summarized in Table 3 based on all selected cases. It is seen that the void has the most pronounced effects as it directly determines whether cracking occurs. The second important feature is the phase state, as it determines the local stress state so as to influence the damage behaviours of IGB (recall Fig. 10). The crystallographic orientation is estimated to be the less important feature. Due to this reason, the specified crystallographic orientations in Sections 4.2 and 4.3 do not affect the obtained cracking mechanisms.

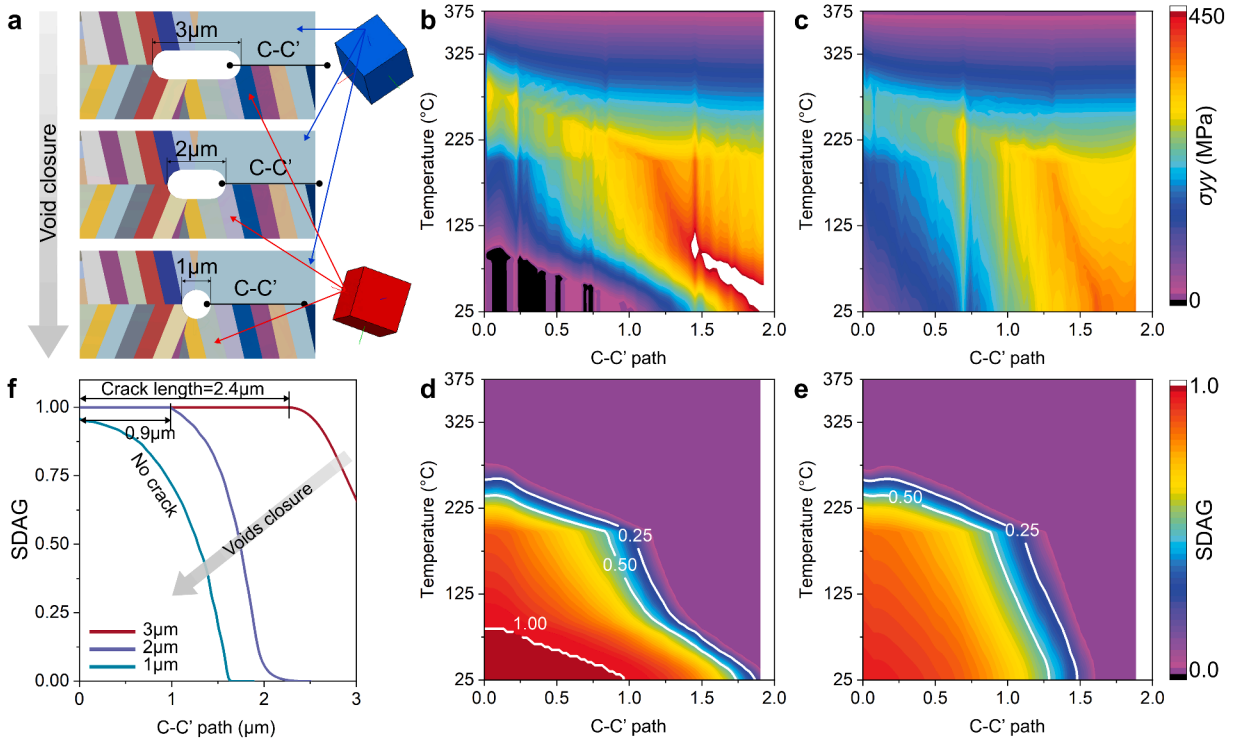

Fig. 14. Effects of void closure on IGB cracking: (a) models with three lengths of voids, (b) evolution of σ_{yy} with 2μm void, (c) evolution of σ_{yy} with 1μm void, (d) evolution of SDAG with 2μm void, (e) evolution of SDAG with 1μm void, (f) comparison of SDAG obtained after the cooling process among three models.

6. Conclusions

A CPFE-CZM coupled model is developed to provide fundamental insights into thermal cracking in diffusion-bonded 9Cr-1Mo steel. The CPFE-CZM is a micromechanical model reflecting the effects of microstructural variables, such as voids, phases and GBs, on thermal cracking. By examining the 9Cr-1Mo steel fabricated through diffusion bonding, the effects of an interfacial void and its length, GB migration and grain orientation were quantitively analysed and compared. The main conclusions are summarised below:

1. Characterisation results indicate that the high fraction of voids gives rise to more Interfacial Grain Boundary (IGB) cracking. The stress at void-free IGB between martensite and ferrite is dominated by the shear stress, the magnitude of which is too small to initiate a crack. The existence of voids at IGB induces considerably higher normal stress, which is the main cause of IGB cracking.
2. Characterisation results show that the presence of martensite in the grains with migrated GB can stop the interfacial cracking, while the ferrite grains are more susceptible to cracking. The computational results reproduced this phenomenon and pointed out that high normal tensile stresses are developed inside ferrite grains during cooling, which may pave the way for cracking and eventual fracture. On the contrary, limited normal tensile stress was developed in martensite, which thus shows high cracking resistance.
3. By controlling the microstructure variables (e.g., grain orientation) in computational modelling, the effects of length of void on IGB cracking are isolated and discussed. Under the selected conditions, results show that the length of the crack is three times shorter when the void length shrinks from 3μm to 2μm. No cracking occurs if a void is less than 1μm.
4. The computational model provides a quantitative analysis of the effects of individual microstructure features. It was found that the void has the most pronounced effects on thermal cracking, followed by phase state, while the crystallographic orientation is less important parameter.

CRediT authorship contribution statement

Wei Wang: Conceptualization, Data curation, Formal analysis, Investigation, Software, Validation, Writing – original draft, Writing – review & editing. **Ruiqiang Zhang:** Formal analysis, Investigation, Methodology. **Amir A Shirzadi:** Methodology, Investigation, Formal analysis, Writing – review & editing. **Daniel S Balint:** Formal analysis, Writing – review & editing. **Lee Aucott:** Resources, Formal analysis, Writing – review & editing. **Jun Jiang:** Conceptualization, Formal analysis, Funding acquisition, Methodology, Supervision, Writing – original draft, Writing – review & editing.

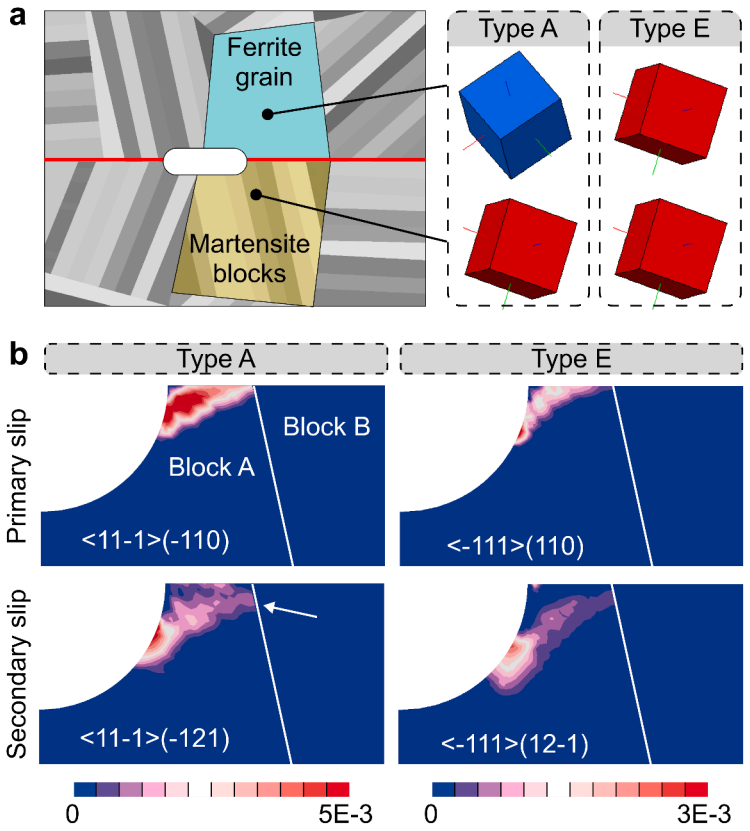

Fig. 15. Model details in discussing crystallographic effects: (a) grain orientations in Type A and Type E, (b) primary and secondary slip field in Type A and Type E.

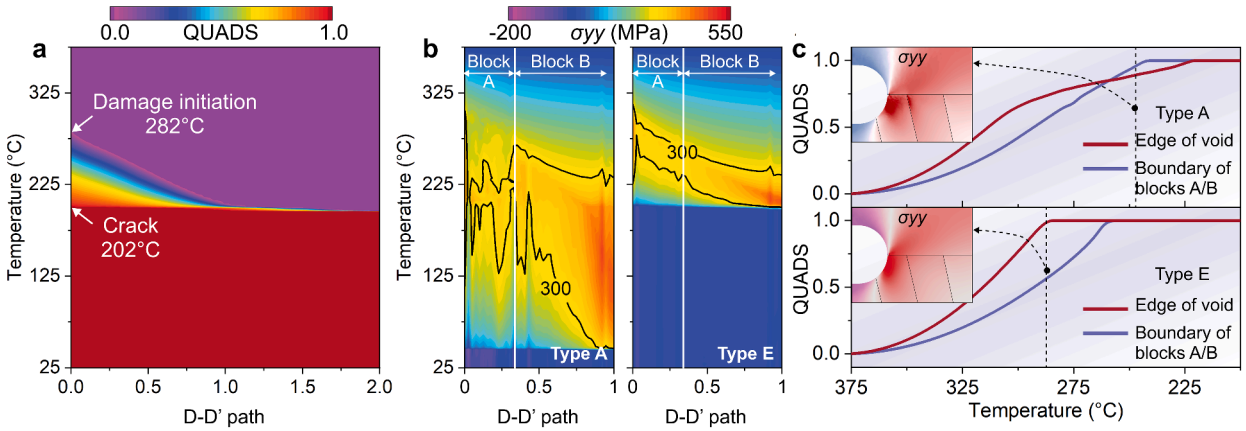

Fig. 16. Comparison of IGB damage behaviour in Type A and Type E: (a) QUADS in Type E, (b) σ_{yy} in Type A and Type E, (c) QUADS at void boundary and boundary of Block A/B.

Table 2
Euler angle and misorientation.

	Type A	Type E	3	4	5	6	7	8
Grain A	195.6, 33.9, 21.5	104.9, 19.7, 56.9	113, 32, 7					
Grain B	104.9, 19.7, 56.9	104.9, 19.7, 56.9	104, 30, 6	97, 29, 3.5	75, 34, 18	56, 38,30	36, 50, 35	40, 53, 16
Misorientation			10°	20°	30°	40°	50°	60°

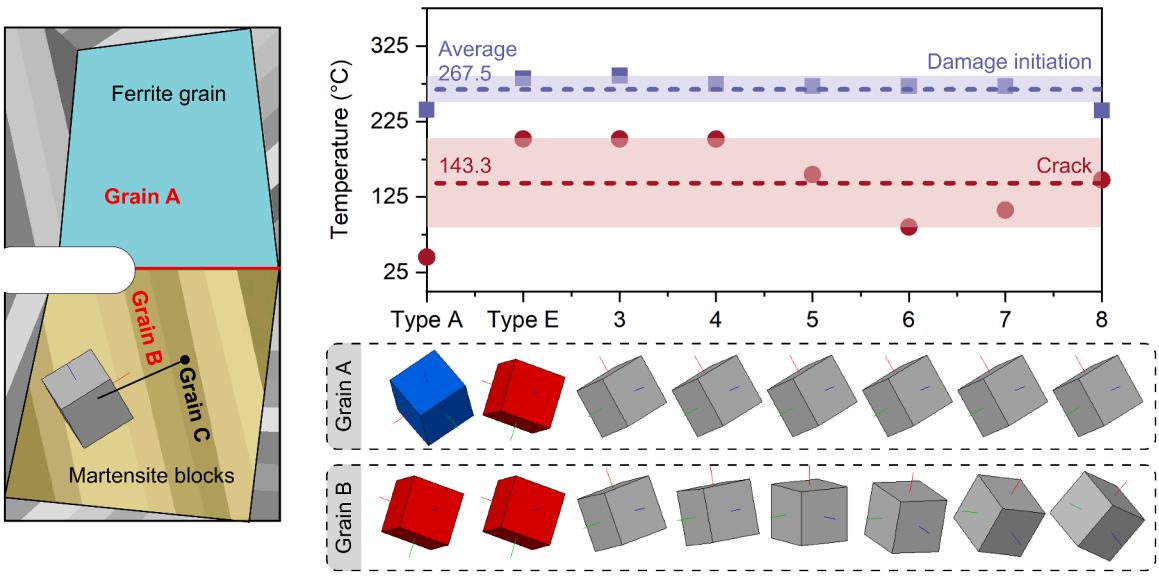

Fig. 17. Crystallographic sensitivity of IGB damaging and cracking.

Table 3
Effects of microstructure features on IGB cracking.

	Length of void	Phase state	Grain orientation
Length of crack-best case	No crack (Fig. 7)	2.7μm (Type A)	2.7μm (Type A)
Temperature of cracking-best case	No crack (Fig. 7)	45 °C (Type A)	45 °C (Type A)
Length of crack-worst case	2.7μm (Type A)	4.1μm (Type B)	2.9μm (Type E)
Temperature of cracking-worst case	45 °C (Type A)	275 °C (Type B)	202 °C (Type E)

Declaration of competing interest

The authors declare that they have no known competing financial interests or personal relationships that could have appeared to influence the work reported in this paper.

Data availability

Data will be made available on request.

Acknowledgements

WW gratefully acknowledges the China Scholarship Council (grant number 202006050025) for financial support through the Imperial-CSC scholarship scheme. This work has been part-funded by the EPSRC Energy Programme (grant number EP/W006839/1).

Appendix A

To validate the modelling strategy, the stress distributions are compared between the quasi-3D model and the 3D model, as shown in Fig. A1. The shear stress among all four examined cases remains the same, which has been proven to be insufficient to nucleate cracks. The normal stress distributions show dependence on the adjacent grain (ferrite or martensite), but the general trend does not change, that is: the IGB show significantly higher normal stress than shear stress. Thus, the conclusions obtained by quasi-3D modelling would not be affected. Considering the complex grain morphology of ferrite and martensite, the three-dimensional modelling would induce tremendous variables such as the relative position of the microstructure features, including voids, martensite phase and ferrite phase. Therefore, the quasi-3D finite element model was used and the effects of phase distribution in the third dimension were beyond the aim of this work.

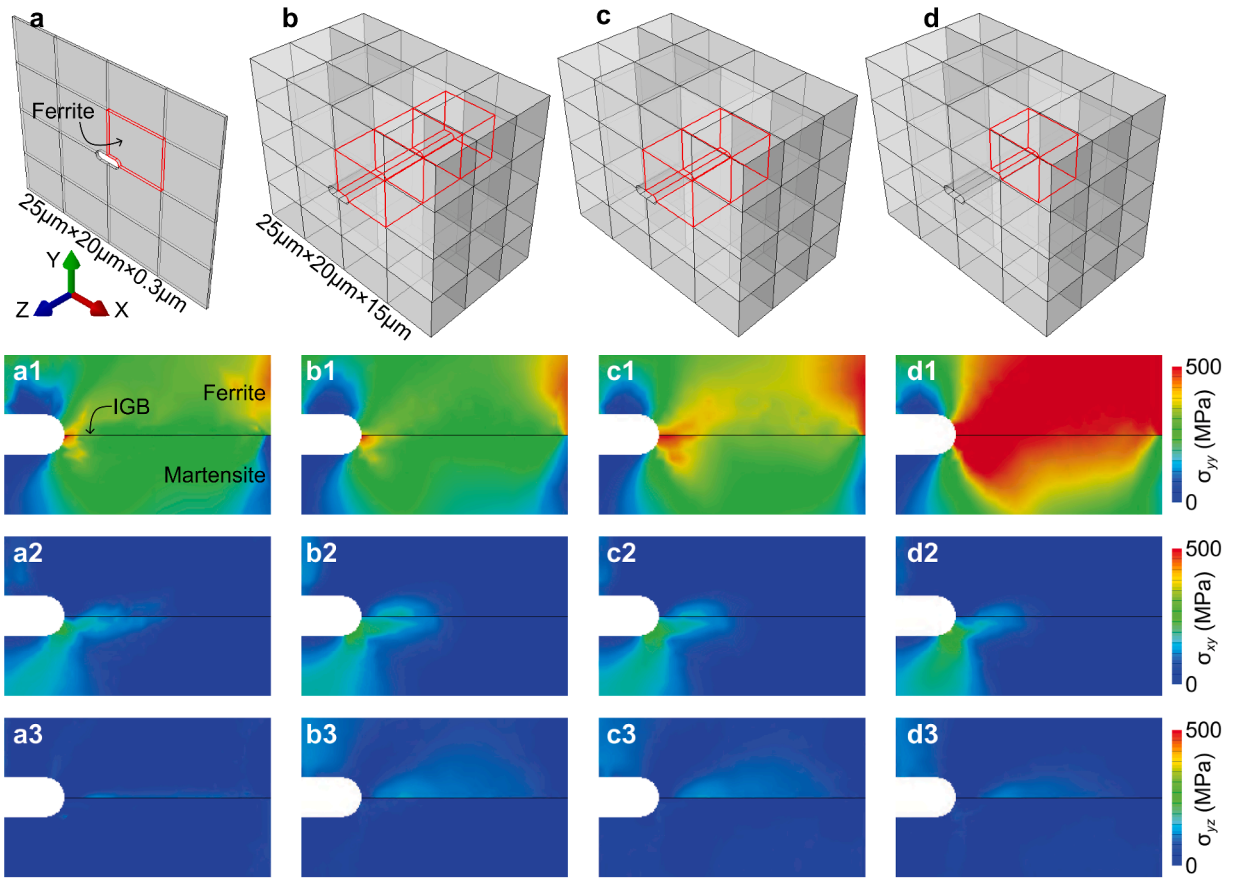

Fig. A1. Compare the stress distributions between quasi-3D model and 3D model. (a) is quasi-3D model, (b), (c) and (d) show 3D model with different phase distributions in the third dimension.

References

Alabort, E., Barba, D., Sulzer, S., Lißner, M., Petrinic, N., Reed, R.C., 2018. Grain boundary properties of a nickel-based superalloy: characterisation and modelling. Acta Mater. 151, 377–394. https://doi.org/10.1016/j.actamat.2018.03.059, 2018/06/01.

Arsenlis, A., Parks, D.M., 1999. Crystallographic aspects of geometrically-necessary and statistically-stored dislocation density. Acta Mater. 47 (5), 1597–1611. https://doi.org/10.1016/S1359-6454(99)00020-8, 1999/03/31.

Basuki, W.W., Kraft, O., Aktaa, J., 2012. Optimization of solid-state diffusion bonding of Hastelloy C-22 for micro heat exchanger applications by coupling of experiments and simulations. Mater. Sci. Eng.: A 538, 340–348. https://doi.org/10.1016/j.msea.2012.01.056, 2012/03/15.

Cai, W., Sun, C., Wang, C., Qian, L., Li, Y., Fu, M.W., 2022. Modelling of the intergranular fracture of TWIP steels working at high temperature by using CZM–CPFE method. Int. J. Plast. 156, 103366 https://doi.org/10.1016/j.ijplas.2022.103366, 2022/09/01.

Caillard, D., Martin, J.L., 2003. Thermally Activated Mechanisms in Crystal Plasticity. Elsevier.

Chatterjee, A., Chakrabarti, D., Moitra, A., Mitra, R., Bhaduri, A.K., 2014. Effect of normalization temperatures on ductile–brittle transition temperature of a modified 9Cr–1Mo steel. Mater. Sci. Eng.: A 618, 219–231. https://doi.org/10.1016/j.msea.2014.09.021, 2014/11/17.

Chen, X., Deng, X., Sutton, M.A., 2013. Simulation of stable tearing crack growth events using the cohesive zone model approach. Eng. Fract. Mech. 99, 223–238. https://doi.org/10.1016/j.engfracmech.2012.12.017, 2013/02/01.

Chen, J., Liu, C., Wei, C., Liu, Y., Li, H., 2019. Study on microstructure and mechanical properties of direct diffusion bonded low-carbon RAFM steels. J. Manuf. Process. 43, 192–199. https://doi.org/10.1016/j.jmapro.2019.05.020, 2019/07/01.

Cheng, J., Ghosh, S., 2015. A crystal plasticity FE model for deformation with twin nucleation in magnesium alloys. Int. J. Plast. 67, 148–170. https://doi.org/10.1016/j.ijplas.2014.10.005, 2015/04/01.

Chu, K., et al., 2010. Thermal conductivity of SPS consolidated Cu/diamond composites with Cr-coated diamond particles. J. Alloys. Compd. 490 (1), 453–458. https://doi.org/10.1016/j.jallcom.2009.10.040, 2010/02/04.

Dunne, F.P.E., Rugg, D., Walker, A., 2007. Lengthscale-dependent, elastically anisotropic, physically-based hcp crystal plasticity: application to cold-dwell fatigue in Ti alloys. Int. J. Plast. 23 (6), 1061–1083. https://doi.org/10.1016/j.ijplas.2006.10.013, 2007/06/01.

Erdogan, M., Priestner, R., 1999. Effect of epitaxial ferrite on yielding and plastic flow in dual phase steel in tension and compression. Mater. Sci. Technol. 15 (11), 1273–1284. https://doi.org/10.1179/026708399101505383, 1999/11/01.

Fillafer, A., Werner, E., Krempaszky, C., 2017. On phase transformation induced effects controlling the initial flow behavior of ferritic-martensitic dual-phase steels. Mater. Sci. Eng.: A 708, 556–562. https://doi.org/10.1016/j.msea.2017.10.005, 2017/12/21.

Ghoncheh, M.H., et al., 2020. On the solidification characteristics, deformation, and functionally graded interfaces in additively manufactured hybrid aluminum alloys. Int. J. Plast. 133, 102840 https://doi.org/10.1016/j.ijplas.2020.102840, 2020/10/01.

Hill, A., Wallach, E.R., 1989. Modelling solid-state diffusion bonding. Acta Metallurgica 37 (9), 2425–2437. https://doi.org/10.1016/0001-6160(89)90040-0, 1989/09/01.
Hwang, E.H., Park, J.S., Kim, S.O., Seong, H.G., Kim, S.J., 2020. Study on the controlling factors for the quenching crack sensitivity of ultra-strong automotive steel. J. Mater. Sci. 55 (8), 3605–3617. https://doi.org/10.1007/s10853-019-04177-1, 2020/03/01.
Kang, S.H., Im, Y.T., 2007. Thermo-elasto-plastic finite element analysis of quenching process of carbon steel. J. Mater. Process. Technol. 192-193, 381–390. https://doi.org/10.1016/j.jmatprotec.2007.04.101, 2007/10/01.
Kazakov, N.F., 2013. Diffusion Bonding of Materials. Elsevier.
Krauss, G., 1999. Martensite in steel: strength and structure. Mater. Sci. Eng.: A 273-275, 40–57. https://doi.org/10.1016/S0921-5093(99)00288-9, 1999/12/15.
Lee, T.L., et al., 2018. Modelling and neutron diffraction characterization of the interfacial bonding of spray formed dissimilar steels. Acta Mater. 155, 318–330. https://doi.org/10.1016/j.actamat.2018.05.055, 2018/08/15.
Li, H., Chandra, N., 2003. Analysis of crack growth and crack-tip plasticity in ductile materials using cohesive zone models. Int. J. Plast. 19 (6), 849–882. https://doi.org/10.1016/S0749-6419(02)00008-6, 2003/06/01.
Li, M., Sun, F., Li, D.F., O'Donoghue, P.E., Leen, S.B., O'Dowd, N.P., 2018. The effect of ferrite phases on the micromechanical response and crack initiation in the intercritical heat-affected zone of a welded 9Cr martensitic steel. Fatigue Fract. Eng. Mater. Struct. 41 (6), 1245–1259. https://doi.org/10.1111/ffe.12768, 2018/06/01.
Mahler, M., Aktaa, J., 2015. Approach for J–R curve determination based on sub-size specimens using a triaxiality dependent cohesive zone model on a (ferritic–martensitic) steel. Eng. Fract. Mech. 144, 222–237. https://doi.org/10.1016/j.engfracmech.2015.06.086, 2015/08/01.
Mahler, M., Aktaa, J., 2016. Prediction of fracture toughness based on experiments with sub-size specimens in the brittle and ductile regimes. J. Nucl. Mater. 472, 178–185. https://doi.org/10.1016/j.jnucmat.2015.08.046, 2016/04/15.
Manchiraju, S., Anderson, P.M., 2010. Coupling between martensitic phase transformations and plasticity: a microstructure-based finite element model. Int. J. Plast. 26 (10), 1508–1526. https://doi.org/10.1016/j.ijplas.2010.01.009, 2010/10/01.
Marvi-Mashhadi, M., Vaz-Romero, A., Sket, F., Rodríguez-Martínez, J.A., 2021. Finite element analysis to determine the role of porosity in dynamic localization and fragmentation: application to porous microstructures obtained from additively manufactured materials. Int. J. Plast. 143, 102999 https://doi.org/10.1016/j.ijplas.2021.102999, 2021/08/01.
Mazul, I.V., et al., 2016. Technological challenges at ITER plasma facing components production in Russia. Fusion Eng. Des. 109-111, 1028–1034. https://doi.org/10.1016/j.fusengdes.2016.01.030, 2016/11/01.
McCarthy, O.J., McGarry, J.P., Leen, S.B., 2014. The effect of grain orientation on fretting fatigue plasticity and life prediction. Tribol. Int. 76, 100–115. https://doi.org/10.1016/j.triboint.2013.09.023, 2014/08/01.
Moore, J.A., Rusch, J.P., Nezhad, P.S., Manchiraju, S., Erdeniz, D., 2023. Effects of martensitic phase transformation on fatigue indicator parameters determined by a crystal plasticity model. Int. J. Fatigue 168, 107457. https://doi.org/10.1016/j.ijfatigue.2022.107457, 2023/03/01.
Ozturk, D., Shahba, A., Ghosh, S., 2016. Crystal plasticity FE study of the effect of thermo-mechanical loading on fatigue crack nucleation in titanium alloys. Fatigue Fract. Eng. Mater. Struct. 39 (6), 752–769. https://doi.org/10.1111/ffe.12410, 2016/06/01.
Paramatmuni, C., Guo, Y., Withers, P.J., Dunne, F.P.E., 2021. A three-dimensional mechanistic study of the drivers of classical twin nucleation and variant selection in Mg alloys: a mesoscale modelling and experimental study. Int. J. Plast. 143, 103027 https://doi.org/10.1016/j.ijplas.2021.103027, 2021/08/01.
Pinz, M., Benzing, J.T., Pilchak, A., Ghosh, S., 2022. A microstructure-based porous crystal plasticity FE model for additively manufactured Ti-6Al-4V alloys. Int. J. Plast. 153, 103254 https://doi.org/10.1016/j.ijplas.2022.103254, 2022/06/01.
Quey, R., Dawson, P.R., Barbe, F., 2011. Large-scale 3D random polycrystals for the finite element method: generation, meshing and remeshing. Comput. Methods Appl. Mech. Eng. 200 (17), 1729–1745. https://doi.org/10.1016/j.cma.2011.01.002, 2011/04/01.
Schröder, R., 1985. Influences on development of thermal and residual stresses in quenched steel cylinders of different dimensions. Mater. Sci. Technol. 1 (10), 754–764. https://doi.org/10.1179/mst.1985.1.10.754, 1985/10/01.
Simonovski, I., Cizelj, L., 2013. Cohesive element approach to grain level modelling of intergranular cracking. Eng. Fract. Mech. 110, 364–377. https://doi.org/10.1016/j.engfracmech.2013.05.011, 2013/09/01.
Singh, A., Pal, S., 2020. Coupled chemo-mechanical modeling of fracture in polycrystalline cathode for lithium-ion battery. Int. J. Plast. 127, 102636 https://doi.org/10.1016/j.ijplas.2019.11.015, 2020/04/01.
Sugianto, A., Narazaki, M., Kogawara, M., Shirayori, A., Kim, S.Y., Kubota, S., 2009. Numerical simulation and experimental verification of carburizing-quenching process of SCr420H steel helical gear. J. Mater. Process. Technol. 209 (7), 3597–3609. https://doi.org/10.1016/j.jmatprotec.2008.08.017, 2009/04/01.
Suiker, A.S.J., Turteltaub, S., 2005. Computational modelling of plasticity induced by martensitic phase transformations. Int. J. Numer. Methods Eng. 63 (12), 1655–1693. https://doi.org/10.1002/nme.1327, 2005/07/28.
Suman, S., Biswas, P., 2020. Comparative study on SAW welding induced distortion and residual stresses of CSEF steel considering solid state phase transformation and preheating. J. Manuf. Process. 51, 19–30. https://doi.org/10.1016/j.jmapro.2020.01.012, 2020/03/01.
Suman, S., Biswas, P., 2021. Finite element analysis of in- process thermal mitigation of welding induced residual stresses in 9Cr-1Mo-V steel butt joint considering phase transformation. J. Manuf. Process. 70, 361–375. https://doi.org/10.1016/j.jmapro.2021.08.027, 2021/10/01.
Tandogan, I.T., Yalcinkaya, T., 2022. Development and implementation of a micromechanically motivated cohesive zone model for ductile fracture. Int. J. Plast. 158, 103427 https://doi.org/10.1016/j.ijplas.2022.103427, 2022/11/01.
Tasan, C.C., et al., 2015. An overview of dual-phase steels: advances in microstructure-oriented processing and micromechanically guided design. Annu. Rev. Mater. Res. 45, 391–431.
Taylor, G.I., 1934. The mechanism of plastic deformation of crystals. Part II.—comparison with observations. Proc. R. Soc. Lond. Ser. A, Contain. Paper. Math. Phys. Character 145 (855), 388–404. https://doi.org/10.1098/rspa.1934.0107, 1934/07/02.
Vishnu, A.R., Vadillo, G., Rodríguez-Martínez, J.A., 2023. Void growth in ductile materials with realistic porous microstructures. Int. J. Plast. 167, 103655 https://doi.org/10.1016/j.ijplas.2023.103655, 2023/08/01.
Voothaluru, R., Bedekar, V., Xie, Q., Stoica, A.D., Hyde, R.S., An, K., 2018. In-situ neutron diffraction and crystal plasticity finite element modeling to study the kinematic stability of retained austenite in bearing steels. Mater. Sci. Eng.: A 711, 579–587. https://doi.org/10.1016/j.msea.2017.11.069, 2018/01/10.
Wang, W., et al., 2023. Imparted benefits on mechanical properties by achieving grain boundary migration across voids. Acta Mater. 256, 119103 https://doi.org/10.1016/j.actamat.2023.119103, 2023/09/01.
Wilson, D., Wan, W., Dunne, F.P.E., 2019. Microstructurally-sensitive fatigue crack growth in HCP, BCC and FCC polycrystals. J. Mech. Phys. Solids. 126, 204–225. https://doi.org/10.1016/j.jmps.2019.02.012, 2019/05/01.
Xie, M., et al., 2022. A dual-phase crystal plasticity finite-element method for modeling the uniaxial deformation behaviors of thermally aged SAC305 solder. Int. J. Plast. 155, 103342 https://doi.org/10.1016/j.ijplas.2022.103342, 2022/08/01.
Xu, X.P., Needleman, A., 1993. Void nucleation by inclusion debonding in a crystal matrix. Model. Simul. Mat. Sci. Eng. 1 (2), 111.
Xu, Y., et al., 2021. Intermetallic size and morphology effects on creep rate of Sn-3Ag-0.5Cu solder. Int. J. Plast. 137, 102904 https://doi.org/10.1016/j.ijplas.2020.102904, 2021/02/01.
Xu, Y., et al., 2022. A multi-scale approach to microstructure-sensitive thermal fatigue in solder joints. Int. J. Plast. 155, 103308 https://doi.org/10.1016/j.ijplas.2022.103308, 2022/08/01.
Yaghi, A.H., Hyde, T.H., Becker, A.A., Sun, W., 2007. Numerical simulation of P91 pipe welding including the effects of solid-state phase transformation on residual stresses. Proc. Inst. Mech. Eng. Part L: J. Mater.: Des. Appl. 221 (4), 213–224. https://doi.org/10.1243/14644207JMDA152, 2007/10/01.
Yaghi, A.H., Hyde, T.H., Becker, A.A., Sun, W., 2008. Finite element simulation of welding and residual stresses in a P91 steel pipe incorporating solid-state phase transformation and post-weld heat treatment. J. Strain. Anal. Eng. Des. 43 (5), 275–293. https://doi.org/10.1243/03093247JSA372, 2008/05/01.
Yaghi, A.H., Hyde, T.H., Becker, A.A., Sun, W., 2013. Finite element simulation of residual stresses induced by the dissimilar welding of a P92 steel pipe with weld metal IN625. Int. J.Pressure Vessel. Pip. 111-112, 173–186. https://doi.org/10.1016/j.ijpvp.2013.07.002, 2013/11/01.

Zhang, C., Li, H., Li, M.Q., 2015. Interaction mechanism between void and interface grain boundary in diffusion bonding. Sci. Technol. Weld. Join. 20 (2), 123–129. https://doi.org/10.1179/1362171814Y.0000000242, 2015/02/01.

Zhang, T., Jiang, J., Britton, B., Shollock, B., Dunne, F., 2016. Crack nucleation using combined crystal plasticity modelling, high-resolution digital image correlation and high-resolution electron backscatter diffraction in a superalloy containing non-metallic inclusions under fatigue. Proc. R. Soc. A: Math. Phys. Eng. Sci. 472 (2189), 20150792 https://doi.org/10.1098/rspa.2015.0792, 2016/05/01.

Zhang, Z., Lunt, D., Abdolvand, H., Wilkinson, A.J., Preuss, M., Dunne, F.P.E., 2018. Quantitative investigation of micro slip and localization in polycrystalline materials under uniaxial tension. Int. J. Plast. 108, 88–106. https://doi.org/10.1016/j.ijplas.2018.04.014, 2018/09/01.

Zheng, Z., Eisenlohr, P., Bieler, T.R., Pagan, D.C., Dunne, F.P.E., 2020. Heterogeneous internal strain evolution in commercial purity titanium due to anisotropic coefficients of thermal expansion. JOM 72 (1), 39–47. https://doi.org/10.1007/s11837-019-03743-x, 2020/01/01.

Zuo, Y., Zhao, C., Robador, A., Wickham, M., Mannan, S.H., 2022. Quasi-in-situ observation of the grain growth and grain boundary movement in sintered Cu nanoparticle interconnects. Acta Mater. 236, 118135 https://doi.org/10.1016/j.actamat.2022.118135, 2022/09/01.